Crystal-chemical, vibrational and electronic properties of 1M-phlogopite K(Mg,Fe)3Si3AlO10(OH)2 from Density Functional Theory simulations

Crystal-chemical, vibrational and electronic properties of 1*M*-phlogopite $K(Mg,Fe)_3Si_3AlO_{10}(OH)_2$ from Density Functional Theory simulations

Gianfranco Ulian[1], Giovanni Valdrè[1,*]

1 Dipartimento di Scienze Biologiche, Geologiche e Ambientali, Centro di Ricerche Interdisciplinari di Biomineralogia, Cristallografia e Biomateriali, Università di Bologna "Alma Mater Studiorum" Piazza di Porta San Donato 1, 40126 Bologna, Italy.

** Corresponding author: Giovanni Valdrè (giovanni.valdre@unibo.it)*

Abstract

Trioctahedral micas are peculiar minerals that may present interesting electronic properties that can be modulated by specific cationic substitutions. In the present work, a detailed characterization of the structural, vibrational, and electronic properties of 1*M*-phlogopite as a function of the Fe^{II}/Mg^{II} substitutions, with Mg/Fe ratio ≥ 2, is reported. The results were obtained from density functional theory simulations at the B3LYP-D* level of theory, which included the effect of long-range interactions, and also using all-electron Gaussian-type orbitals to describe the atoms in the mineral. The crystal structures of the different phlogopite models were in good agreement with previous X-ray and neutron diffraction data reported in the literature. In addition, the simulated Raman spectra well described the experimental ones obtained from confocal Raman micro-spectrometry, providing additional information on the atomic motions. The electronic band structure and the atom- and orbital-projected density of states were also discussed, describing the nature of the band gap and electronic transitions, and how they vary with the iron content.

Keywords

1*M*-phlogopite; crystal structure; IR and Raman spectroscopy; electronic properties; Density Functional Theory

1. Introduction

Micas belong to the phyllosilicate family, whose general formula is $AM_{2-3}T_4O_{10}X_2$, where A = K, Na, Ca is the interlayer cation, M = Mg, Al, Fe is the octahedral cation, T = Si and Al is the tetrahedral cation, and X = OH, F, Cl, O. These layered minerals are structurally characterized by an octahedral (O) sheet sandwiched between two tetrahedral (T) sheets forming a packet called 2:1 layer, T–O–T, or TOT. These layers are negatively charged because of the presence of Al^{III}/Si^{IV} substitutions in the T sheets, which are balanced by the presence of monovalent or divalent cations in the interlayer region. The crystal structure is thus given by strong covalent/ionic bonds within the TOT layers on the *ab* crystallographic plane, which in turn are stacked and held together by a mix of ionic and dispersive interactions along the [001] direction (Ventruti et al., 2009).

From the geological perspective, phlogopite and biotite are ubiquitous minerals found in various and manyfold rocks in igneous, sedimentary, and metamorphic environments (Icenhower and London, 1995). Like other phyllosilicates, the presence of hydroxyl groups within the crystal structure makes them important water reservoirs for the release and storage of H_2O in the Earth's mantle (Virgo and Popp, 2000), which may affect several petrologic processes because of the variations of melting conditions and other properties of the sub-crustal material (Ventruti et al., 2009). It is worth remembering that phlogopite is also a source of K_2O that concurs in the generation of potassium-rich magmas in the upper mantle (Tutti et al., 2000).

In addition to their wide and well-known use in ceramics and glass (Ariane et al., 2023; Ercenk and Yilmaz, 2015; Faeghinia and Razavi, 2016; King et al., 2000), trioctahedral micas could be interesting dielectric materials in optoelectronic applications because of their large band gap of about 5–6 eV (Frisenda et al., 2020), which could be modulated by the amount of iron or other cation/anion substituents (Meunier et al., 1983). This was indeed demonstrated by the earlier experiments of Davidson and Yoffe (1968), who showed that the electrical conductivity in trioctahedral mica is a bulk-controlled process related to the presence of transition metals (mainly Fe and Ti) in the octahedral sheet.

The electronic properties of phlogopite were never computationally investigated in detail because of the low symmetry of the structure and the relatively high computational demands. The only available work was carried out within the density functional theory (DFT) framework, with simulations conducted using the B3LYP functional and all-electron atomic basis sets (Timon et al., 2013). They considered several Fe^{II}/Mg^{II}

substitutions between 0 and 100% of the available cationic sites, however they did not include any correction for the long-range interactions that are severely underestimated within the standard DFT framework.

In addition, in the scientific literature there are no reports regarding the theoretical infrared (IR) and Raman spectra of this mineral, and how the spectra vary with the iron content. This information is of fundamental importance for the interpretation of experimental data. For example, in the study of Moro et al. (2017) it was found in the Raman spectrum of the phlogopite sample BU1-7 a triplet of bands in the 600 – 800 cm^{-1}, whereas only one band should be present. According to previous investigations, the presence of three bands is due to high iron contents in the mineral (Wang et al., 2015). However, the spectroscopic results on the BU1-7 sample analysed by Moro and collaborators (2017) are not in line with the previous statement, because the cited specimen has low Fe content.

The present work is focused on trioctahedral micas, *i.e.*, those presenting magnesium in the octahedral sheet, which typically show an extended solid solution between the Mg and Fe end-members, phlogopite (Phl) $KMg_3(Si_3Al)O_{10}(OH)_2$ and annite (Ann) $KFe_3(Si_3Al)O_{10}(OH)_2$, respectively. To be noted that iron can be present both as a divalent cation in the octahedral sheet and as a trivalent one in the T sheet, as shown by Mössbauer spectroscopy (Scordari et al., 2012). Conventionally, phlogopites have Mg/Fe ratio > 2, whereas biotite has Mg/Fe ratio < 2 (Deer et al., 1992). In nature, trioctahedral micas commonly crystallize as 1*M* polytype (see **Fig.1**), which may coexist with other polytypes such as the $2M_1$, as described by Lacalamita and co-workers (2012).

To extend and complete the knowledge of phlogopite, in this paper a detailed characterization of the 1*M* polytype of phlogopite using DFT-based simulations is provided. Specifically, the crystal structure, the vibrational spectra, and electronic properties (band structure and density of states) of phlogopite are reported as a function of the iron(II) content in the octahedral sheet, which were compared and discussed in detail against previous experimental and few theoretical data.

2. Materials and Methods

2.1 Computational methods

The Density Functional Theory simulations were performed using the CRYSTAL17 code (Dovesi et al., 2018), employing the hybrid B3LYP functional, which uses the Becke 3-parameters exchange functional (Becke, 1993) in combination with the correlation one of Lee, Yang and Parr (Lee et al., 1988). This functional, which includes 20% of exact Hartree-Fock exchange and some non-local contribution to the exchange-correlation terms, is well-known for its accuracy when simulating the structural, elastic, dielectric (optical) and vibrational properties of minerals and solids (Pascale et al., 2004; Pascale et al., 2005). In addition, it was already used to model the properties of other phyllosilicates, e.g., talc (Ulian et al., 2013) and muscovite (Ulian and Valdrè, 2015a), obtaining data in very good agreement with the experimental findings. As mentioned in the introduction, most DFT functionals lack of proper treatment of the long-range interactions, which were however here accounted for by the semiempirical correction DFT-D2 (Grimme, 2006), specifically reparametrized for the B3LYP functional. This combination is called B3LYP-D* approach in the scientific literature (Civalleri et al., 2008).

Kohn-Sham orbitals were described within the linear combination of atomic orbitals (LCAO) approach, using all-electron Gaussian-type functions for each atom in the structure. The selected atomic basis sets were 88-31G* for Si (Nada et al., 1996), 85-11G* for Al (Catti et al., 1994), 8-511d1G for Mg (Valenzano et al., 2007), 86-511G for K (Dovesi et al., 1991), 8-411d11G for O (Valenzano et al., 2007), 3-1p1G for H (Gatti et al., 1994), and 86-411d41G for Fe (Catti et al., 1995). These all-electron basis sets were already recently employed in the study of the structural, elastic, vibrational and thermodynamic properties of other phyllosilicates such as talc (Ulian et al., 2014), pyrophyllite (Ulian and Valdrè, 2015b), muscovite (Ulian and Valdrè, 2015a) and clinochlore (Ulian et al., 2018, 2020).

The accuracy of the Coulomb and exchange series were controlled by five thresholds set to 10^{-8} (ITOL1 to ITOL4) and 10^{-16} (ITOL5) for structural relaxation and to 10^{-10} and 10^{-20} when calculating the dielectric and polarizability tensors (*vide infra*). The reciprocal space was sampled with a 5×5×5 Monkhorst–Pack mesh (Monkhorst and Pack, 1976), corresponding to 39 independent *k* points. The CRYSTAL default pruned grid (75 radial, 974 angular points, XLGRID) was used to calculate the total energy of the system, via numerical

integration of the electron density over the unit cell volume (Dovesi et al., 2018). The self-consistent-field (SCF) convergence on energy was set to 10^{-8} Hartree and 10^{-10} Hartree for geometry optimization and vibrational frequency calculation, respectively.

Zone-central (*i.e.*, Γ-point) normal modes were calculated by diagonalizing the mass-weighted Hessian matrix *W* (dynamical matrix), whose elements are the second derivatives of the lattice potential for mass-weighted atomic displacements (Pascale et al., 2004):

$$W_{\alpha i,\beta j}(\Gamma) = \frac{H_{\alpha i,\beta j}}{\sqrt{M_\alpha M_\beta}},$$

with $H_{\alpha i,\beta j}$ the energy second derivative, M_α and M_β the atomic masses and the subscripts in Latin (i, j) and in Greek letters (α, β) the atomic coordinates and the atoms, respectively. The infrared intensities were calculated analytically in terms of absorbance, using the classical absorption formula as explained by Maschio et al. (2012):

$$A(\nu) = \frac{1}{3}\sum_{ii=1}^{3}\frac{4\pi}{\lambda\rho}\mathrm{Im}\left[n_{ii}(\nu)\right]$$

where the terms $A(\nu)$, λ, ρ, and n are the infrared absorption, the wavelength of the incident light, the mineral density and the complex refractive index, respectively. This absorption formula reproduces in a satisfactorily way the typical shape of the bands observed in IR spectroscopy. The polarization direction is expressed by the subscripts ii. The real and imaginary parts of the refractive index n_{ii} were obtained from the following relations:

$$\left\{\mathrm{Re}\left[n_{ii}(\nu)\right]\right\}^2 - \left\{\mathrm{Im}\left[n_{ii}(\nu)\right]\right\}^2 = \mathrm{Re}\left[\epsilon_{ii}(\nu)\right]$$

$$2\,\mathrm{Re}\left[n_{ii}(\nu)\right]\cdot\mathrm{Im}\left[n_{ii}(\nu)\right] = \mathrm{Im}\left[\epsilon_{ii}(\nu)\right]$$

The term $\epsilon_{ii}(\nu)$ is the complex dielectric tensor, which was computed for each inequivalent polarization direction according to a classical Drude-Lorentz model:

$$\epsilon_{ii}(\nu) = \epsilon_{\infty,ii} + \sum_p \frac{f_{p,ii}\nu_p^2}{\nu_p^2 - \nu^2 - i\nu d_p}.$$

with ϵ_∞ the optical (high frequency) dielectric tensor, ν_p the transverse optical frequency, f_p the oscillator strength and d_p the damping factor of the p^{th} vibrational mode. As suggested by Maschio and co-workers

(2012), to obtain a band broadening similar to those typically found in experimental samples, the damping factor (*i.e.*, the full width at half maximum of each vibrational mode) was set to 8.

The Raman intensities were instead calculated within the Placzek (1934) approximation assuming the mineral as a polycrystalline powder, by using the optical vibrational modes employing a pseudo-Voigt functional form (Maschio et al., 2013a, b):

$$A(\nu) = \eta L(\nu) + (1-\eta) G(\nu)$$

where, in this case, $A(\nu)$ represents the Raman intensity and $L(\nu)$ and $G(\nu)$ are given by:

$$L(\nu) = \sum_p \frac{I_p}{\pi} \frac{\varphi_p/2}{\left(\nu - \nu_p\right)^2 + \left(\varphi_p/2\right)^2}$$

$$G(\nu) = \sum_p 2\sqrt{\frac{\ln 2}{\pi}} \frac{I_p}{\varphi_p} \exp\left[-\frac{4\ln 2 \left(\nu - \nu_p\right)^2}{\varphi_p^2} \right]$$

with I_p the computed Raman intensity and φ_p the full width at half maximum for the p^{th} vibrational mode, and η the Lorentz factor. A pure Lorentzian form, which is the default of CRYSTAL (Maschio et al., 2013a), corresponding to $\eta = 1$, was employed to obtain the typical sharp bands of Raman spectra as explained by Dovesi et al. (2018). The Raman intensity of the p^{th} mode was calculated according to the following formula:

$$I_p \propto C \left(\frac{\alpha}{\partial Q_p} \right)^2$$

where α is the polarizability, Q_p is the normal mode coordinate for mode p. C is a prefactor that depends on the (angular) frequency of the exciting laser ω_L and the temperature T according to:

$$C \sim \left(\omega_L - \omega_p\right)^4 \frac{1}{30\omega_p} \left[1 - \exp\left(-\frac{\hbar \omega_p}{k_B T} \right) \right]^{-1}$$

with k_B the Boltzmann's constant and ω_p the angular frequency of mode p. In the simulations, the prefactor was calculated setting T = 298 K and ω_L = 532 nm to mimic the experimental conditions (*vide infra*). All the tensorial properties related to the intensity of the bands in the infrared and Raman spectra, *i.e.*, the dielectric tensor, and the polarizability, were calculated analytically using a Couple Perturbed Kohn-Sham (CPKS) approach (Ferrero et al., 2008a; Ferrero et al., 2008b).

2.2 Experimental methods

The 1*M*-phlogopite single-crystal sample BU1-7 used in the present study was extracted from the BU1 rock, which is from the deposits of the Bunyampaka maar (Kasenyi field). According to the analyses of Stoppa and collaborators (2003), the rock was a melilitite bomb described as a lapilli tuffisite that presents 20% subhedral phlogopite crystals associated with 40% olivine, 25% melilite and 15% spinel. The crystal chemistry of the BU1-7 sample was previously characterized by Lacalamita and co-workers (2012) using electron probe microanalysis, Mössbauer spectroscopy and single-crystal X-ray diffraction. The mineral belonged to the *C*2/*m* space group (monoclinic system), with lattice parameters a = 5.3259(2) Å, b = 9.2245(3) Å, c = 19.2309(4) Å and β = 100.050(2) °, with two unit formulas (Z = 2) of $(K_{0.90}Na_{0.05}Ba_{0.01})[Mg_{2.34}Al_{0.08}Fe(II)_{0.20}Fe(III)_{0.08}Ti_{0.26}Cr_{0.05}][Si_{2.87}Al_{1.07}Fe(III)_{0.06}]O_{10.58}(F_{0.10}OH_{1.31})$ in the crystallographic cell.

Several Raman spectra were collected at room temperature (~20°C) using a WITec Alpha 300R confocal Raman microscopy system, made of an optical microscope and an ultra-high throughput UHTS 300 VIS spectrometer with CCD camera and gratings of 600 g/mm. A green laser beam (532 nm) was used as excitation light, setting a power of 30 mW to prevent heating the sample and possible alterations on the mineral. The laser beam was focused on the sample with a 100× Zeiss microscope objective with a low numerical aperture objective (NA = 0.50) to avoid optical artefacts. The backscattered Raman spectra were collected in confocal mode between 100 and 4000 cm^{-1}, with a resolution of about 2.7 cm^{-1} and an acquisition time of 10 minutes. The Rayleigh scattering line was removed by an edge filter.

3. Results and discussion

3.1 Phlogopite crystal structure

The neutron diffraction results of Ventruti and collaborators (Ventruti et al., 2009; Ventruti et al., 2008) were employed to create the model of the 1*M* polytype of phlogopite. The crystal structure was experimentally refined with relatively high symmetry (space group *C*2/*m*) due to the partial occupancies of the cationic sites with different atoms. For example, in the experimental structure there was a single, symmetrically inequivalent tetrahedral site that generates all the TO_4 units in the unit cell (4 sites in the primitive cell) due to the symmetry elements of the *C*2/*m* space group. This T site is occupied by about 70% by Si and 30% by Al (Ventruti et al.,

2009), meaning that, randomly, 1/4 sites are occupied by aluminium. However, in quantum mechanical simulations, each site must have single occupancy, for example, a T site may be occupied by either Al or Si but not by both at the same time. To both include the Al^{III}/Si^{IV} substitutions in the T sheets and preserve the monoclinic structure, an analysis of the sub-groups of the experimentally determined crystals was performed, finding that, for phlogopite with chemical formula $K(Mg,Fe)_3(AlSi_3)O_{10}(OH)_2$, the 1*M* polytype can be described in the *P*2 space group (44 atoms in the unit cell, $Z = 2$, 26 inequivalent by symmetry). Within this setting, there were four inequivalent tetrahedral sites, of which those containing Si^{IV} were labelled as T1–T3 and the one with aluminium as T4, and six non-equivalent cationic sites in the octahedral sheet, labelled as M1–M6. Hence, due to symmetry, each T site was related to two SiO_4 or AlO_4 tetrahedra, one in one tetrahedral sheet and one in the other of the TOT layer, whereas all octahedral sites are symmetrically independent. In stoichiometric $KMg_3(AlSi_3)O_{10}(OH)_2$, whose model was labelled Phl-Fe0, all M sites were occupied by magnesium, whereas in the ferroan phlogopite structure with chemical formula $KMg_{2.5}Fe_{0.5}(AlSi_3)O_{10}(OH)_2$ (called Phl-Fe1) the site M4 contained Fe, and in the model $KMg_2Fe(AlSi_3)O_{10}(OH)_2$ (Phl-Fe2) the sites M1 and M4 presented Fe^{II}/Mg^{II} substitutions. These sites were chosen because they ensure a sufficient distance between the iron atoms in the mineral structure (see **Fig.1**). The authors are aware that this was one of the possible ways to place the desired atomic substitutions within the phlogopite unit cell. For example, a simple combinatorics analysis showed that there were 16 ways (i.e., inequivalent configurations) to place two Al^{III}/Si^{IV} substitutions in the tetrahedral sheet. Further complexity due to placing iron in the octahedral sheet dramatically increases the number of possible configurations, which would not be treatable without very large computing resources. It is expected that different configurations could lead to slightly different crystal-chemical results, with the general behaviour given by the structurally disordered structure, which is a mean of all the possible configurations weighted on their relative stability (i.e., the energy associated to each configuration). Obviously, the precision of the simulations, in terms of a better comparison with the experimental data, would increase by considering more configurations, i.e., by fully addressing the structural disorder.

The crystallographic features, *i.e.*, lattice parameters, tetrahedral (T) and octahedral (M) sheet thicknesses, interlayer space (I), and selected polyhedral properties were reported in **Table 1**, alongside previous XRD and neutron scattering results (Lacalamita et al., 2012; Ventruti et al., 2009). Simulated powder X-ray

diffractograms, obtained from the optimized phlogopite models, are plotted in **Fig.2**, alongside the XRD pattern obtained from the refinements of a phlogopite sample at 10 K by Ventruti and collaborators (2009). These diffractograms were obtained considering a standard Cu Kα radiation. As expected, the most intense reflection was the one at about 8° 2θ related to the (001) plane. It was observed that the Fe^{II}/Mg^{II} substitutions caused slight variations in both the position and intensity of some reflections. **Table 2** showed the mean bond and interlayer distances for each cationic site, and complete data on specific atom bond distances could be found in **Table S1** in the Supplementary Materials. In the structural analysis, three types of oxygen atoms were distinguished, i.e., basal oxygen, O(b), apical oxygen, O(a) and hydroxyl oxygen, O(h). Basal oxygen atoms are those shared with other SiO_4 tetrahedra, whereas the apical ones are those involved in the bonding between the T and O sheets. The structural comparison with the single-crystal XRD data was performed considering the BU1-1 sample reported by Lacalamita and collaborators (2012) because the authors reported more structural details (bond lengths and angles) for this sample than those of the BU1-7 specimen. However, the differences in the lattice constants between the two samples were very small (see the Materials and Methods section), thus it can be assumed that the internal geometries would be similar.

The theoretical results were generally in line with the experimental data reported in the literature, with a very low underestimation of the unit cell volume ($\Delta V \leq -1.5\%$). In agreement with previous simulations on dioctahedral muscovite (Ulian and Valdrè, 2015a), it was of utmost importance to include long-range interactions to properly consider and describe the properties of phyllosilicates. In the present work, the DFT-D* approach led to unit cell volumes that were smaller than the experimental ones, in good agreement with the crystallographic refinements. The Fe^{II}/Mg^{II} cationic substitutions in the octahedral sheet resulted in a continuous decrease of the moduli of the lattice vectors, hence in the shrinking of the unit cell volume. The value of the 001 reflection decreased in the order Phl-Fe0 (10.046 Å) > Phl-Fe1 (10.036 Å) > Phl-Fe2 (10.020 Å), as can be noted in **Fig.2**. The reduced size of the phlogopite unit cell with increasing iron content in the O sheet was due to a variation of the forces (bond strength) in the site where Fe^{II}/Mg^{II} substitutions occurred, as observed from the analysis of the charge density difference of the phlogopite models. This analysis was graphically reported in **Fig.3**, calculated on a plane perpendicular to the [001] direction and passing through the cations in the octahedral sheet. Indeed, in the Phl-Fe0 structure (**Fig.3a**), the charge density is negative (meaning that electric charges are carried away) around the M^{II} cations, and it is positive (meaning electrons

are concentrated) on and between the oxygen atoms. This result suggested the ionic nature of the bonds between the involved atoms. In addition, a slightly more positive charge density was noticed on the O(a) bonded to the Al^{III} atoms in the tetrahedral sheet, in line with the increased negative charge on the AlO_4 tetrahedra with respect to the SiO_4 ones. The iron substitutions led to (i) an increase of the positive charge on the O(a) and O(h) atoms and (ii) a small decrease of the radius of negative charge density around the Fe^{III} ion. As a result, the O sheet thickness is reduced due to the M – O bond shortening, especially in the M1 and M4 sites (see **Table 2**). At the same time, there is a very small increase of the interlayer thickness. This could suggest the presence of slightly lower interaction between the TOT layers and the interlayer cations in the iron-bearing phlogopite than in the stoichiometric model, resulting in an easier cleavage of the (001) planes of the mineral. The observed unit cell volume variations were in contrast with the structural data reported by Timon et al. (2013), who performed DFT/B3LYP simulations with the CRYSTAL09 code and obtained an increasing length of the *b* and *c* lattice parameters, with the **a** vector remaining almost constant. This means that the unit cell volume of phlogopite increased with the amount of iron in the octahedral sheet, according to the results of Timon and collaborators (2013). Despite the similar theoretical approach, this different behaviour could be due, most probably, to the absence of any correction for long-range interactions. Albeit the DFT-D2 scheme was implemented in CRYSTAL09, the cited authors did not include van der Waals interactions because they considered the bonding between the (negatively charged) TOT layers and the (positively charged) interlayer cations as mainly ionic. Instead, it was recently showed the relevancy of the dispersive forces for the characterization of the crystal structure, vibrational properties and thermodynamics of muscovite $KAl_2Si_3AlO_{10}(OH)_2$, the dioctahedral equivalent of phlogopite, where long-range interactions play a fundamental role (Ulian and Valdrè, 2015a). Furthermore, other computational settings could influence the results and the discrepancy. For example, Timon et al. (2013) used a smaller basis set for the oxygen atom (6-31d1) than that employed by us (8-411d11G). Also, tighter tolerances for the bi-electronic and Coulomb integrals and a sampling grid in the reciprocal space with 39 *k*-points were set in the present work (see Materials and Methods), whereas the cited authors used larger tolerances (10^{-7} and 10^{-14}) and a smaller *k* grid with 36 points in the reciprocal space. All these parameters concurred to the determination of the total energy of the system, which in turn affected the forces calculated during the unit cell relaxation.

Besides the necessary approximations introduced in the DFT simulations (e.g., the absence of thermal effects, the Born-Oppenheimer approximation, and numeric algorithms), the differences between the present theoretical simulations and the experimental results can be ascribed to the mineral composition. In this work, both stoichiometric and Fe-bearing 1*M*-phlogopite models with general formula $K(Mg,Fe)_3(AlSi_3)O_{10}(OH)_2$ were modelled and geometrically optimized, whereas the experimental samples presented several cationic/anionic substitutions. For example, the neutron diffraction experiments of Ventruti et al. (2009) were conducted on a phlogopite sample whose formula was $(K_{0.86}Na_{0.08}Ba_{0.04})$ $[Mg_{1.97}Fe(II)_{0.29}Fe(III)_{0.37}Ti_{0.19}Al_{0.17}Mn_{0.01}]$ $(Si_{2.72}Al_{1.28})O_{10}(OH)_{1.22}F_{0.12}$, as calculated from a combination of electron probe microanalysis (EPMA), CHN analysis and Mössbauer spectroscopy. The presence of cations and anions with ionic radii that are different from those of the substituted elements, and the site vacancies were expected to deeply affect the crystal structure. The theoretical results suggested that the inclusion of iron in the octahedral sheet caused a reduction of the unit cell volume of the mineral, which was due to an overall contraction of the lattice vectors of about 0.4%.

The DFT results were also in good agreement with the experimental refinements made by Brigatti and collaborators (1996), who performed single-crystal XRD refinements on several phlogopite samples collected from the Tapira carbonatite complex in Brazil. The selected sample, Tas 27-2Ba, had a chemical composition close to the ideal Phl-Fe0 model, with very low amounts of Fe and Ti in the octahedral sheet. A fine comparison was also made on the single crystal investigated by Comodi et al. (2004), which was collected from Colli Albani in Italy. As previously observed for the other experimental samples, the present results showed a slightly smaller unit cell volume than that obtained from the XRD analyses.

The mean atomic charges calculated for each atom in the different phlogopite-1*M* models from the analysis of the Born charge tensor were reported in **Table S2** (Supporting Information), whose values were close to the formal oxidation states (q_K = +1 |*e*|, q_{Mg} = +2 |*e*|, q_{Si} = +4 |*e*|, q_{Al} = +3 |*e*|, q_{Fe} = +2 |*e*|, q_H = +1 |*e*|, q_O = –2 |*e*|). It is worth noting that when the atom – atom bond is not purely ionic, i.e., it has some covalent contribution, the atomic charges deviate from the ideality, but the formal charge of the ions are generally respected. For example, the O(h) and H atoms presented about –1.3 and +0.3 charges, respectively, but the hydroxyl group having the expected –1 charge.

3.2 Infrared and Raman spectra

Each crystalline material has an associated number of degrees of freedom equal to three times the atoms in the unit cell (3*N*), which give the so-called total irreducible representation (IRREP), Γ_{tot}. Three of these 3*N* modes are related to acoustic vibrations (Γ_a), whereas the other $3N - 3$ are optical modes (Γ_o). In both standard IR and Raman spectroscopies, the IRREP is calculated in the central zone of the Brillouin zone (Γ point), hence the Γ_a modes have a zero-frequency value. The phlogopite-1*M* models here employed belonged to the *P*2 space group and their point group was C_2 (2). Since it contains 44 atoms in the unit cell, this polytype of phlogopite has 132 modes, whose IRREP was calculated as:

$$\Gamma_{tot} = \Gamma_a + \Gamma_o = 62A + 70B,$$

with $A + 2B$ acoustic modes (Γ_a) and $61A + 68B$ optical modes (Γ_o), the latter being active in both infrared and Raman spectroscopies.

The site symmetry analysis (see **Table 3**) for the 1*M* polytype was in line with that of McKeown and collaborators (1999). It is worth noting that the factor group analysis reported by the cited authors is related to the phase belonging to the *C*2/*m* space group, whereas the present analysis was performed considering the *P*2 symmetry. Thus, in this space group setting, all vibrational modes are active in both IR and Raman spectroscopies. Furthermore, McKeown et al. (1999) considered the hydroxyl site as a single contributor, *i.e.*, it counted as a single atom and excluded the effect of O – H stretching modes. It is worth remembering that the density functional theory data are generally blue-shifted (higher wavenumbers) because of the absence of any thermal effect and the harmonic approximation, which typically increases the force constants of the computed vibrational modes. The calculation of the infrared and Raman spectra of (Fe-bearing) phlogopite at $T = 298$ K would require the knowledge of the thermal behaviour of the mineral, in particular the unit cell volume at room temperature, which can be accessed from the volumetric and axial thermal expansion coefficients. This information could be obtained, for example, from quasi-harmonic approximation simulations, *i.e.*, by knowing how the phonon frequencies vary with volume (pressure), which are computationally demanding and beyond the scope of the present work. However, albeit thermal effects were neglected, the theoretical results at zero Kelvin are comparable with the experimental ones having in mind

313 that, within the selected computational approach, the vibrational bands were generally blue-shifted, and were
314 helpful in assigning each band to specific lattice vibrations.

315 The calculated vibrational wavenumbers ν for the modes with *A* and *B* IRREP are reported in **Tables 4** and **5**,
316 respectively. The *A* modes were also subject to the longitudinal optical (LO) - transverse optical (TO) splitting,
317 which is common in many layered silicates where atoms that vibrate perpendicularly to the layers (the so-
318 called polar modes, or Fröhlich modes) should vibrate at their longitudinal optical frequency (Balan et al.,
319 2001). The LO-TO splitting associated with the *A* modes was reported in **Table 4**. For the sake of
320 completeness, the complex dielectric function, the refractive index and the reflectance spectra along the *x*, *y*
321 and *z* Cartesian directions were also calculated and reported in **Tables S3 – S5** in the Supporting Information.
322 In the following, to better present and discuss the results, the infrared and Raman spectra were treated
323 separately. It is worth recalling also that the experimental spectra were obtained at room temperature (298 K),
324 whereas the theoretical ones at absolute zero (0 K). Thermal effects were included only in the Raman spectra
325 for the calculation of the intensity of the bands (see Materials and Methods for further details).

326 A representative experimental Raman spectrum of the phlogopite sample BU1-7 obtained from confocal
327 Raman micro-spectrometry was reported in **Fig.4a** (black line) in the spectral range 90 – 1200 cm^{-1}, together
328 with the DFT data on the Phl-Fe0 (blue line), Phl-Fe1 (red line) and Phl-Fe2 (green line) models. Full spectra
329 in the range 90 – 3900 cm^{-1} can be found in a dedicated dataset freely available online (Ulian and Valdrè,
330 2023). The assignment of the Raman bands to specific phonon modes was performed with the aid of the
331 potential energy distribution (PED) obtained from theoretical simulations and using the previous results
332 reported in the literature (Moro et al., 2017). At high Raman shifts, there was a single band with low intensity
333 at 3706 cm^{-1} in the experimental spectrum, related to the O – H stretching mode (not shown in **Fig.4a** for the
334 sake of clarity). The same band was observed at about 3760 cm^{-1} in the theoretical Raman spectra, as obtained
335 from the correction proposed by Tosoni and collaborators (2005) to include the anharmonicity to this specific
336 kind of normal mode.

337 In the experimental spectrum, there were two very broad, low intensity bands centred at 915 and 1075 cm^{-1}
338 related to the antisymmetric Si–O stretching (ν_a SiO_4). In fact, the DFT simulations showed the presence of
339 several modes, with eight asymmetric Si – O(b) + Si – O(a) stretching modes (3*B* + 5*A*) that fell in the range

1000 – 1100 cm^{-1}, whereas the range 900 – 1000 cm^{-1} presented eleven bands (7*B* + 4*A*) mainly due to the contribution of Si – O(a) stretching motions. The theoretical intensity of these bands was very low, suggesting that the two experimental bands could be due to the overlap of these signals, explaining their broadness.

The range 650 – 800 cm^{-1} in the experimental spectra was characterized by a triplet of slightly broad bands centred at 674 cm^{-1}, 738 cm^{-1} and 778 cm^{-1}, in agreement with the previous results of Moro et al. (2017). The analysis of the PED showed that the first experimental band was due to the combination of two strong bands calculated at 686 cm^{-1} and 707 cm^{-1}, related to symmetric "umbrella" O(b) – Si – O(a) and O(b) – Al – O(a) bending modes, confirming the analysis of McKeown and collaborators (1999), who measured these umbrella modes at 684 cm^{-1} and 712 cm^{-1}, respectively. There were also other modes contributing to this band, which were due to the combination of the umbrella motions with Mg – O(h) – H (and Fe – O – H in the iron-bearing phlogopite models) bending modes, commonly called O–H librations. The bands at 738 cm^{-1} and 778 cm^{-1} were due to symmetric Si–O(b) stretching modes (ν_s SiO_4), which also saw the contribution of O–H libration modes. This intermix of the Si – O(b) modes with the Mg/Fe – O(h) – H ones caused a slight increase of the intensity of these bands in the iron-bearing phlogopite models. It is possible suggesting that this effect was due to the variation of the polarizability of the Fe – O(h) bonds with respect to the Mg – O(h) ones. Indeed, the intensity of the Raman bands is proportional to the square of the variation of the polarizability of the system during the atomic vibration. However, there is a disagreement between the intensity of the signals obtained from the DFT simulations and the experimental ones, being very high. As explained in the introduction, Wang et al. (2015) suggested that these two signals should have quite low intensities, which could increase because of specific cationic substitutions in the octahedral sheet. The simulations of the Fe-bearing models seem to confirm this hypothesis, with the band at 783 cm^{-1} increasing the intensity (see **Fig.4**), but not as high as observed in the experimental spectrum. Since the BU1-7 sample presented also a quite large amount of titanium in the octahedral sheet, the Fe + Ti content could justify the increase of the intensity of these two bands, as already explained by Moro and co-workers (2017). In addition, the slight intermix of the Si – O(b) modes with the Mg/Fe – O(h) – H ones caused a slight variation of the position of the vibrational bands.

According to the theoretical PED analysis, the modes with the most contribution of hydroxyl librations fell in the range 600 – 650 cm^{-1}, with very low Raman intensities, with the most intense band found at 636 cm^{-1}. In

the experimental spectrum, no band was found correlated to this specific mode. However, the DFT spectral range of the Mg – O(h) – H bending modes was highly affected by anharmonicity, as also discussed in previous work on talc (Ulian et al., 2013). Unfortunately, the used version of the CRYSTAL code did not allow to correct the anharmonic behaviour of OH libration modes, but it is expected these bands would fall at lower wavenumbers than those calculated.

Lattice modes fell in the spectral range below 550 cm^{-1}, and they were due to different kinds of atomic vibrations, in particular long-range T_4O_{10} sheet motions mixed with octahedral cations and hydroxyl group displacements. In the experimental Raman spectrum, there were quite broad signals at 533 cm^{-1}, 422 cm^{-1} and 347 cm^{-1}, an intense and narrow band at 187 cm^{-1}, two shoulders at 320 cm^{-1} and 147 cm^{-1}, and three small bands at 289 cm^{-1}, 264 cm^{-1} and 78 cm^{-1}. Mg – O(a) and Mg – O(h) stretching modes were calculated within DFT at 530 cm^{-1} and 456 cm^{-1}, respectively. Si – O(a) – Mg bending modes occur in the spectral range 470 – 510 cm^{-1}, whereas the O – Mg – O bending modes fall between 345 cm^{-1} and 434 cm^{-1}. These theoretical bands had very low intensity in Raman, in agreement with the experimental measurement. The strong theoretical bands at about 205 cm^{-1} and 180 cm^{-1} were associated with a symmetric and collective Mg – O(a) – Mg bending (resulting in the compression of the interlayer space) and the rotations of the SiO_4 tetrahedra around a shared vertex, respectively. These bands were found in the experimental Raman spectrum at about 187 cm^{-1} and 147 cm^{-1}, respectively, in line with the modes observed by McKeown and co-workers (1999), i.e., 162 cm^{-1} and 105 cm^{-1}, respectively. The small band at about 114 cm^{-1} was composed of two almost degenerate phonon modes related to the sliding of the TOT layers along the *x* and *y* directions. The present DFT results for the stoichiometric Phl-Fe0 model were also in line with the Raman spectrum of a fluorine-poor phlogopite of formula $(K_{0.911}Na_{0.047})(Mg_{2.723}Fe_{0.026}Al_{0.111}Ti_{0.062}Cr_{0.002}Ni_{0.001})(Si_{2.955}Al_{1.045})O_{10}(OH_{1.954}F_{0.053}Cl_{0.002})$, whose most relevant bands were centred at 193 cm^{-1}, 281 cm^{-1}, 327 cm^{-1}, 358 cm^{-1}, 682 cm^{-1} (Sun et al., 2022).

In general, the presence of increasing amounts of divalent iron in the octahedral sheet results in low ($|\Delta\nu| < 10$ cm^{-1}) spectral shifts for modes involving the octahedral cations, e.g., Fe – O(a) and Fe – O(h) modes between 200 – 250 cm^{-1}, whereas smaller shifts ($|\Delta\nu| < 1$ cm^{-1}) were observed for modes not mainly related to the O sheet. This also led to some bands showing a change in intensity, e.g., those at 204 cm^{-1} and 214 cm^{-1}, because

of the combined red- and blue-shifts, i.e., shifts at lower and higher wavenumbers, respectively. Generally, the bands are more shifted when the related phonon modes directly involve the iron cations, e.g., Fe – O(a) and Fe – O(h) modes. This led to different overlaps or separations of the bands, which resulted in the presence of more low-intensity bands or fewer high-intensity signals, respectively.

The DFT simulated infrared spectra of the Phl-Fe0, Phl-Fe1, and Phl-Fe2 models were reported in **Fig.4b** as blue, red and green lines, respectively. As a general observation, the bands that were very intense in the Raman spectrum are weaker in the IR spectrum, and vice versa. The *P*2 space group used to model phlogopite does not contain the inversion centre as the *C*2/*m* one observed from the experimental refinements, hence the mutual exclusion rule did not apply. In general, small differences can be noted in the spectra with increasing iron content, especially in the spectral region above 500 cm^{-1}. The change in intensity and position of some bands are due to the same reasons explained for the Raman spectra. Considering the systematic blue-shift imposed by the harmonic approximation, our results were in good agreement with the experimental findings of Jenkins (1989) in the spectral range 1300 – 350 cm^{-1} for a natural phlogopite mineral with chemical composition near ideality, i.e., $K_{0.72}(Mg_{2.85}Al_{0.14})(Al_{0.87}Si_{3.13})O_{10}(OH,F)_2$ (spectrum drawn with a black line in **Fig.4b**). In the theoretical spectra, the most intense bands for $v < 1200$ cm^{-1} fell at 935 cm^{-1} and 976 cm^{-1} for symmetric Si – O(a), 945 cm^{-1} and 999 cm^{-1} for symmetric Si – O(b) and 1008 cm^{-1} for asymmetric Si – O(a) stretching modes. The band with medium intensity at 1067 cm^{-1} and the very low-intensity one at 1100 cm^{-1} in the DFT spectra were associated to asymmetric Si – O(b) stretching modes. Jenkins (1989) described a broad band centred at 995 cm^{-1} in the experimental IR spectrum, which was generally assigned to the Si – O stretching vibrations, without specifying the type of oxygen atom (apical or basal) associated to the vibrational motion. The same band was instead measured by Weiss and collaborators (2010) at 1006 cm^{-1} on a phlogopite sample with both Fe and Ti in the octahedral sheet.

Jenkins reported the band associated with the OH libration mode, *i.e.*, Mg – O – H, at 592 cm^{-1}, whereas in the present simulations for the Phl-Fe0 model a series of bands between about 600 cm^{-1} and 790 cm^{-1} were found, with the most intense band at 647 cm^{-1}. This blue-shift was due to high anharmonic behaviour of this kind of mode, where the energy separation between the different vibrational levels could not be described properly with the harmonic approximation of atomic vibrations.

Summarizing, **Table 6** reports the most intense bands observed in the experimental Raman and infrared spectra, together with the related DFT bands and their assignment to specific normal modes. It can be noted that the mean absolute deviation between the theoretical and experimental positions of the Raman bands with $\nu > 200$ cm^{-1} is about 3%, whereas for infrared spectroscopy the deviation is smaller (about 2%). This is in line with the results of similar comparisons between DFT simulations at 0 K and room temperature as reported in several scientific publications by various authors (see for instance Pascale et al., 2004; Tosoni et al., 2005; Valenzano et al., 2007). For the sake of completeness, **Fig.S1** reports the simulated Raman spectra of the three phlogopite models, considering different laser polarizations (*xx*, *xy*, *xz*, *yy*, *yz* and *zz*).

3.3 Electronic band structure

The electronic band structure of the three phlogopite-1*M* models was calculated in the Γ–Z–D–B–Γ–A–E–Z–C_2–Y_2–Γ–Z'–D'–B'–Γ–A'–E'–Z'–C'_2–Y'_2–Γ path in the first Brillouin zone (reciprocal lattice). Spin-polarized solutions were also considered due to the presence of Fe^{II} ions with $3d^6$ electronic configuration, which lead to a total spin $S = 2$ (see **Fig.5**). In addition, **Fig.5** reports the atom-projected density of states (DOS) calculated for each model, whereas **Fig.6** shows details of the orbital-projected DOS in the –7.5 – 15 eV for selected atoms.

In each phlogopite model, as in typical insulators, the valence bands were almost flat near the Fermi level (here set to 0 eV). The band gap was of the indirect type, with an energy gap E_g that was very high for the stoichiometric Phl-Fe0 phlogopite (6.94 eV, **Fig.5a**), in line with the experimental value of 7.85 eV calculated from the optical properties by Hendricks and Jefferson (1939). This study is slightly dated, and probably the optical measurements were affected by some uncertainties, explaining the difference of about 1 eV between the theoretical and experimental electronic band gap. Unfortunately, to the authors' knowledge, no recent experimental studies reported band properties for this mineral. The present E_g value was also smaller than that of Timon et al. (2013), who conducted DFT simulations with the CRYSTAL09 code and the hybrid B3LYP functional. As previously explained the different theoretical approach could be the reason of this slight disagreement. From the atom- and orbital-projected density of states, it was possible to note the contribution of the p orbitals of oxygen atoms, especially the apical O(a) ones to the topmost valence bands, whereas the

contribution of all other atoms was negligible between –7.5 eV and the Fermi level. The first conduction bands in the 7 – 10 eV range were mainly due to the hydrogen atoms. For electronic energies greater than 10 eV, the p orbitals of Si were the most contributing element to the conductions bands, followed by the d orbitals of potassium for $E > 12$ eV.

The presence of iron(II) ions in the octahedral sheet of the phyllosilicate led to several important variations in the band structure (see **Figs.5b,c**). First, Fe^{II}/Mg^{II} substitutions reduced the separation between the valence and the conduction bands, an effect that increased with the number of iron ions in the structure. This E_g variation occurred because of the presence of mid-band levels just above the topmost valence band associated with iron (see the atom-projected DOS plots). Moreover, most of the bands associated with the oxygen atoms were shifted at lower energy than the same ones in the Phl-Fe0 model. Also, there were other bands in the conduction region due to Fe^{II}, which crossed the bands associated with H (see the red dashed lines in **Figs.5b,c**). The band gap associated with the α electrons (spin up, or majority-spin) was $E_{g,\alpha} = 5.01$ eV and $E_{g,\alpha} = 4.19$ eV for the phlogopite models with one and two Fe^{II} ions, respectively. When β electrons (spin down, or minority-spin) were considered, the band gap further reduces to $E_{g,\beta} = 3.44$ eV and $E_{g,\beta} = 3.59$ eV for the Phl-Fe1 and Phl-Fe2 models, respectively. The calculated atomic spin density of the Fe4 site in the Phl-Fe1 structure is 3.75 μ_B, whereas the Fe1 and Fe4 sites in the doubly substituted model are both 3.72 μ_B, close to the expected value of 4. The results are also consistent with those of Timon et al. (2013), who calculated a spin density of 3.7 μ_B. Thus, it was possible to modulate the band gap of phlogopite with the amount of iron in the octahedral sheet. This means that it is required less energy to promote the transition of electrons from the valence bands into the conduction ones. For example, in the optics perspective, the mineral can absorb light with different wavelengths (inversely proportional to the E_g value) depending on the amount of iron in the octahedral sheet, hence the mineral could be used for specific applications such as filter screens. The band gap is also relevant in other important applications, e.g., large insulators and semiconducting materials can be used as dielectric and source/drain electrodes, respectively, in field emission transistors.

The analysis of the orbital-projected DOS for the iron(II) substituted structures (**Figs.6c-f**) showed the degeneracy between the 2p orbitals of the O(a) and O(h) atoms and the 3d orbitals (majority spin) of iron in the valence states, and the admixture of the 1s orbital of H and the 3d orbitals (minority spin) of Fe^{II} in the

bottommost conduction bands, with Fe giving the dominant contribution to the electronic bands. The orbitals of O(b) atoms, which are not connected to any iron ion in the octahedral sheet, are not involved in these degenerate levels. This means that these orbital sets, i.e., Fe–O(a), Fe–O(h) and Fe-H, were hybridized and were responsible of the decreasing electronic band gap. These observations agreed with those of Timon and collaborators (2013), with an electronic band gap E_g = 3.70 eV. However, the cited authors calculated a slightly different band structure in the conduction levels, with bands related to the 2p O orbitals placed below those of H. As previously explained, this could be an effect of the different computational parameters.

Finally, for the sake of completeness, the calculated static relative permittivity ε, the refractive index n and the high-frequency relative permittivity ε_{HF} of the different phlogopite models were reported in **Table 7**, which were in good agreement with the available experimental (Bisdom et al., 1982; Gudkov and Metsik, 1973) and theoretical data (Timon et al., 2013). By increasing the amount of iron in phlogopite in place of magnesium, the refractive index and the high-frequency dielectric constant increased as observed in other minerals such as olivine $(Mg, Fe)_2SiO_4$. This effect is due to the increasing density of the mineral with the Fe(II) concentration in phlogopite, which is related to both the volume shrinking and the increasing molecular weight of the unit cell.

4. Conclusions

The present study focused on the crystal-chemical investigation of phlogopite as a function of the iron (Fe^{2+}) content in the octahedral sheet, and how the vibrational and electronic properties vary with the composition. The well-known hybrid functional B3LYP was employed and corrected with the DFT-D2 scheme to properly describe the long-range interactions that typically characterize the layer silicates, together with all-electron basis sets to describe the atomic orbitals. The crystal-chemistry of $KMg_{2-x}Fe_x(Si_3Al)O_{10}(OH)_2$ models, with x = 0, 0.5 and 1 was correctly described by the chosen theoretical framework, finding a general reduction of the unit cell volume by increasing the Fe content in the octahedral sheet of the mineral. The simulated vibrational (infrared and Raman) spectra of phlogopite well reproduced the experimental ones, showing that the triplet of very intense Raman bands here experimentally recorded with confocal Raman micro-spectrometry and in previous works was not only related to the iron content, and that other cationic/anionic substitutions could be

the reason behind the increase of the intensity of two of the three vibrational signals. Further details on the atomic vibrations associated with the specific vibrational modes were also provided as a reference for future experimental and theoretical studies. The electronic band structure and density of states highlighted the progressive reduction of the indirect band gap of the mineral with the number of Fe^{II}/Mg^{II} substitutions, and the strong hybridisations of the 3d Fe – 2p O orbitals in the valence states and of the 3d Fe – 1s H in the conduction bands. This could lead to interesting and peculiar applications of this mineral in optoelectronics because of the wide-bandgap behaviour (E_g > 2 eV) of phlogopite that can be tuned by the number of Fe cations in the octahedral sheet and polarization of the electronic spin. For example, the E_g = 3.49 eV corresponds to a wavelength of about 355 nm, hence this mineral could adsorb (or emit) light radiation in the near ultraviolet. Thus, the mineral could be used as a filter for specific wavelengths, which can be tailored with the concentration of Fe(II) in the octahedral sheet. In future, the effect of Fe^{III}/Mg^{II}, Ti^{IV}/Mg^{II} and Fe^{III}/Si^{IV} will be investigated to increase our understanding of the effects of naturally occurring substitutions in the crystal-chemical and electronic properties of phlogopite. Considering the wide interest in new, sustainable materials for different kinds of applications, phlogopite could be a promising mineral, in particular for two-dimensional optoelectronic devices.

As a final note, this study further assessed the quality of the proposed B3LYP-D*/all-electron basis set approach for the characterization of phyllosilicates with increasing crystal-chemical complexity.

Acknowledgements

The authors wish to thank the University of Bologna supporting the present research. All the simulations were performed with the computational resources (HPC cluster) and software license of the Interdisciplinary Research Centre of Biomineralogy, Crystallography and Biomaterials, Department of Biological, Geological and Environmental Sciences, University of Bologna.

Author Contributions

Conceptualization, G.U. and G.V.; methodology, G.U.; validation, G.U. and G.V.; formal analysis, G.U.; investigation, G.U. and G.V.; data curation, G.U.; writing—review and editing, G.U. and G.V.; visualization, G.U.; supervision, G.V. All authors have read and agreed to the published version of the manuscript.

Data Availability

The results of the present work are reported in the manuscript and in a dedicated dataset published at the following link: https:/doi.org/10.17632/7wsntzztxw.1.

References

Ariane, K., Tamayo, A., Chorfa, A., Rubio, F., Rubio, J., 2023. Optimization of the nucleating agent content for the obtaining of transparent fluormica glass-ceramics. Ceramics International 49, 9826-9838.

Balan, E., Saitta, A.M., Mauri, F., Calas, G., 2001. First-principles modeling of the infrared spectrum of kaolinite. American Mineralogist 86, 1321-1330.

Becke, A.D., 1993. A New Mixing of Hartree-Fock and Local Density-Functional Theories. Journal of Chemical Physics 98, 1372-1377.

Bisdom, E.B.A., Stoops, G., Delvigne, J., Curmi, P., Altemuller, H., 1982. Micromorphology of weathering biotite and its secondary products. Pedologie 32, 225-252.

Brigatti, M.F, Medici, L., Saccani, E., Vaccaro, C., 1996. Crystal chemistry and petrologic significance of Fe^{3+}-rich phlogopite from the Tapira carbonatite complex, Brazil. American Mineralogist, 81, 913-927.

Catti, M., Valerio, G., Dovesi, R., 1995. Theoretical study of electronic, magnetic, and structural properties of a-Fe_2O_3 (hematite). Physical Review B 51, 7441-7450.

Catti, M., Valerio, G., Dovesi, R., Causà, M., 1994. Quantum-mechanical calculation of the solid-state equilibrium MgO + alpha-Al_2O_3 $MgAl_2O_4$ (spinel) versus pressure. Physical Review B 49, 14179-14187.

Civalleri, B., Zicovich-Wilson, C.M., Valenzano, L., Ugliengo, P., 2008. B3LYP augmented with an empirical dispersion term (B3LYP-D*) as applied to molecular crystals. CrystEngComm 10, 405-410.

Comodi, P., Fumagalli, P., Montagnoli, M., Zanazzi, P.F., 2004. A single-crystal study of the pressure behaviour of phlogopite and petrological implications. American Mineralogist 89, 647-653.

554 Davidson, A.T., Yoffe, A.D., 1968. Hopping Electrical Conduction and Thermal Breakdown in Natural and
555 Synthetic Mica. Physica Status Solidi (b) 30, 741-754.
556 Deer, W.A., Howie, R.A., Zussman, J., 1992. An Introduction to the Rock-Forming Minerals, 2nd ed.
557 Longman Group UK Limited, London.
558 Dovesi, R., Erba, A., Orlando, R., Zicovich-Wilson, C.M., Civalleri, B., Maschio, L., Rerat, M., Casassa, S.,
559 Baima, J., Salustro, S., Kirtman, B., 2018. Quantum-mechanical condensed matter simulations with
560 CRYSTAL. Wiley Interdisciplinary Reviews-Computational Molecular Science 8, E1360.
561 Dovesi, R., Roetti, C., Freyria Fava, C., Prencipe, M., Saunders, V.R., 1991. On the elastic properties of
562 lithium, sodium an potassium oxide. An ab initio study. Chemical Physics 156, 11-19.
563 Ercenk, E., Yilmaz, S., 2015. Crystallization kinetics of mica glass-ceramic in the SiO2-Al2O3-MgO-K2O-
564 B2O3-F2system. Journal of Ceramic Processing Research 16, 169-175.
565 Faeghinia, A., Razavi, M., 2016. Microstructural design of phlogopite glass-ceramics. Glass Physics and
566 Chemistry 42, 182-187.
567 Ferrero, M., Rerat, M., Kirtman, B., Dovesi, R., 2008a. Calculation of first and second static
568 hyperpolarizabilities of one- to three-dimensional periodic compounds. Implementation in the CRYSTAL
569 code. Journal of Chemical Physics 129, Art. n. 244110.
570 Ferrero, M., Rerat, M., Orlando, R., Dovesi, R., 2008b. The calculation of static polarizabilities of 1-3D
571 periodic compounds. The implementation in the CRYSTAL code. Journal of Computational Chemistry
572 29, 1450-1459.
573 Frisenda, R., Niu, Y., Gant, P., Muñoz, M., Castellanos-Gomez, A., 2020. Naturally occurring van der Waals
574 materials. npj 2D Materials and Applications 4, Art. n. 38.
575 Gatti, C., Saunders, V.R., Roetti, C., 1994. Crystal-field effects on the topological properties of the electron-
576 density in molecular-crystals - the case of urea. Journal of Chemical Physics 101, 10686-10696.
577 Grimme, S., 2006. Semiempirical GGA-type density functional constructed with a long-range dispersion
578 correction. Journal of Computational Chemistry 27, 1787-1799.
579 Gudkov, O.I., Metsik, M.S., 1973. Dielectric properties of mica at shf. Soviet Physics Journal 16, 664-667.
580 Hendricks, S.B., Jefferson, M.E., 1939. Polymorphism of the micas with optical measurements. American
581 Mineralogist 24, 729-771.

582 Icenhower, J., London, D., 1995. An experimental study of element partitioning among biotite, muscovite,
583 and coexisting peraluminous silicic melt at 200 MPa (H_2O). American Mineralogist 80, 1229-1251.
584 Jenkins, D.M., 1989. Empirical study of the infrared lattice vibrations (1100-350 cm-1) of phlogopite.
585 Physics and Chemistry of Minerals 16, 408-414.
586 King, T.T., Grayeski, W., Cooper, R.F., 2000. Thermochemical reactions and equilibria between fluoromicas
587 and silicate matrices: A petromimetic perspective on structural ceramic composites. Journal of the
588 American Ceramic Society 83, 2287-2296.
589 Lacalamita, M., Mesto, E., Scordari, F., Schingaro, E., 2012. Chemical and structural study of 1M- and 2M
590 (1)-phlogopites coexisting in the same Kasenyi kamafugitic rock (SW Uganda). Physics and Chemistry of
591 Minerals 39, 601-611.
592 Lee, C.T., Yang, W.T., Parr, R.G., 1988. Development of the Colle-Salvetti Correlation-Energy Formula into
593 a Functional of the Electron-Density. Physical Review B 37, 785-789.
594 Maschio, L., Kirtman, B., Orlando, R., Rerat, M., 2012. Ab initio analytical infrared intensities for periodic
595 systems through a coupled perturbed Hartree-Fock/Kohn-Sham method. Journal of Chemical Physics
596 137, Art. n. 204113.
597 Maschio, L., Kirtman, B., Rerat, M., Orlando, R., Dovesi, R., 2013a. Ab initio analytical Raman intensities
598 for periodic systems through a coupled perturbed Hartree-Fock/Kohn-Sham method in an atomic orbital
599 basis. I. Theory. Journal of Chemical Physics 139, Art. n. 164101.
600 Maschio, L., Kirtman, B., Rerat, M., Orlando, R., Dovesi, R., 2013b. Ab initio analytical Raman intensities
601 for periodic systems through a coupled perturbed Hartree-Fock/Kohn-Sham method in an atomic orbital
602 basis. II. Validation and comparison with experiments. Journal of Chemical Physics 139, Art. n.
603 Art. n. 164102.
604 McKeown, D.A., Bell, M.I., Etz, E.S., 1999. Raman spectra and vibrational analysis of the trioctahedral mica
605 phlogopite. American Mineralogist 84, 970-976.
606 Meunier, M., Currie, J.F., Wertheimer, M.R., Yelon, A., 1983. Electrical conduction in biotite micas. Journal
607 of Applied Physics 54, 898-905.
608 Monkhorst, H.J., Pack, J.D., 1976. Special points for Brillouin-zone integrations. Physical Review B 8,
609 5188-5192.

Moro, D., Valdrè, G., Mesto, E., Scordari, F., Lacalamita, M., Della Ventura, G., Bellatreccia, F., Scire, S., Schingaro, E., 2017. Hydrocarbons in phlogopite from Kasenyi kamafugitic rocks (SW Uganda): cross-correlated AFM, confocal microscopy and Raman imaging. Scientific Reports 7, Art. n. 40663.

Nada, R., Nicholas, J.B., McCarthy, M.I., Hess, A.C., 1996. Basis sets for ab initio periodic Hartree-Fock studies of zeolite/adsorbate interactions: He, Ne, and Ar in silica sodalite. International Journal of Quantum Chemistry 60, 809-820.

Pascale, F., Zicovich-Wilson, C.M., Gejo, F.L., Civalleri, B., Orlando, R., Dovesi, R., 2004. The calculation of the vibrational frequencies of crystalline compounds and its implementation in the CRYSTAL code. Journal of Computational Chemistry 25, 888-897.

Pascale, F., Zicovich-Wilson, C.M., Orlando, R., Roetti, C., Ugliengo, P., Dovesi, R., 2005. Vibration frequencies of $Mg_3Al_2Si_3O_{12}$ pyrope. An ab initio study with the CRYSTAL code. Journal of Physical Chemistry B 109, 6146-6152.

Placzek, G., 1934. Handbuch der Radiologie. Akademische Verlagsgeselschft, Leipzig.

Robinson, K., Gibbs, G.V., Ribbe, P.H., 1971. Quadratic elongation: A quantitative measure of distortion in coordination polyhedra. Science 172, 567-570.

Scordari, F., Schingaro, E., Lacalamita, M., Mesto, E., 2012. Crystal chemistry of trioctahedral micas-2M_1 from Bunyaruguru kamafugite (southwest Uganda). American Mineralogist 97, 430-439.

Stoppa, F., Lloyd, F.E., Rosatelli, G., 2003. CO_2 as the propellant of carbonatite-kamafugite cognate pairs and the eruption of diatremic tuffisite. Periodico di Mineralogia 72, 205-222.

Sun, J., Yang, Y., Ingrin, J., Wang, Z., Xia, Q., 2022. Impact of fluorine on the thermal stability of phlogopite. American Mineralogist 107, 815-825.

Timon, V., Praveen, C.S., Escamilla-Roa, E., Valant, M., 2013. Hybrid density functional based study on the band structure of trioctahedral mica and its dependence on the variation of Fe2+ content. Journal of Molecular Graphics & Modelling 44, 129-135.

Tosoni, S., Pascale, F., Ugliengo, P., Orlando, R., Saunders, V.R., Dovesi, R., 2005. Quantum mechanical calculation of the OH vibrational frequency in crystalline solids. Molecular Physiscs 103, 2549-2558.

Tutti, F., Dubrovinsky, L.S., Nygren, M., 2000. High-temperature study and thermal expansion of phlogopite. Physics and Chemistry of Minerals 27, 599-603.

638 Ulian, G., Moro, D., Valdrè, G., 2018. First principle investigation of the mechanical properties of natural
639 layered nanocomposite: Clinochlore as a model system for heterodesmic structures. Composite Structures
640 202, 551-558.
641 Ulian, G., Moro, D., Valdrè, G., 2020. Infrared and Raman spectroscopic features of clinochlore
642 Mg6Si4O10(OH)8: A density functional theory contribution. Applied Clay Science 197, Art. n. 105779.
643 Ulian, G., Tosoni, S., Valdrè, G., 2013. Comparison between Gaussian-type orbitals and plane wave ab initio
644 density functional theory modeling of layer silicates: Talc $Mg_3Si_4O_{10}(OH)_2$ as model system. Journal of
645 Chemical Physics 139, Art. n. 204101.
646 Ulian, G., Tosoni, S., Valdrè, G., 2014. The compressional behaviour and the mechanical properties of talc
647 [$Mg_3Si_4O_{10}(OH)_2$]: a density functional theory investigation. Physics and Chemistry of Minerals 41, 639-
648 650.
649 Ulian, G., Valdrè, G., 2015a. Density functional investigation of the thermo-physical and thermo-chemical
650 properties of 2M(1) muscovite. American Mineralogist 100, 935-944.
651 Ulian, G., Valdrè, G., 2015b. Structural, vibrational and thermophysical properties of pyrophyllite by semi-
652 empirical density functional modelling. Physics and Chemistry of Minerals 42, 609-627.
653 Ulian, G., Valdrè, G., 2023. Crystal-chemical, vibrational and electronic data of 1M-phlogopite, Mendeley
654 Data, V1, doi: 10.17632/7wsntzztxw.1
655 Valenzano, L., Noel, Y., Orlando, R., Zicovich-Wilson, C.M., Ferrero, M., Dovesi, R., 2007. Ab initio
656 vibrational spectra and dielectric properties of carbonates: magnesite, calcite and dolomite. Theoretical
657 Chemistry Accounts 117, 991-1000.
658 Ventruti, G., Levy, D., Pavese, A., Scordari, F., Suard, E., 2009. High-temperature treatment, hydrogen
659 behaviour and cation partitioning of a Fe-Ti bearing volcanic phlogopite by in situ neutron powder
660 diffraction and FTIR spectroscopy. European Journal of Mineralogy 21, 385-396.
661 Ventruti, G., Zema, M., Scordari, F., Pedrazzi, G., 2008. Thermal behavior of a Ti-rich phlogopite from Mt.
662 Vulture (Potenza, Italy): An in situ X-ray single-crystal diffraction study. American Mineralogist 93, 632-
663 643.
664 Virgo, D., Popp, R.K., 2000. Hydrogen deficiency in mantle-derived phlogopites. American Mineralogist 85,
665 753-759.

Wang, A., Freeman, J.J., Jolliff, B.L., 2015. Understanding the Raman spectral features of phyllosilicates. Journal of Raman Spectroscopy 46, 829-845.

Weiss, Y., Kiflawi, I., Navon, O., 2010. IR spectroscopy: Quantitative determination of the mineralogy and bulk composition of fluid microinclusions in diamonds. Chemical Geology 275, 26-34.

List of figures

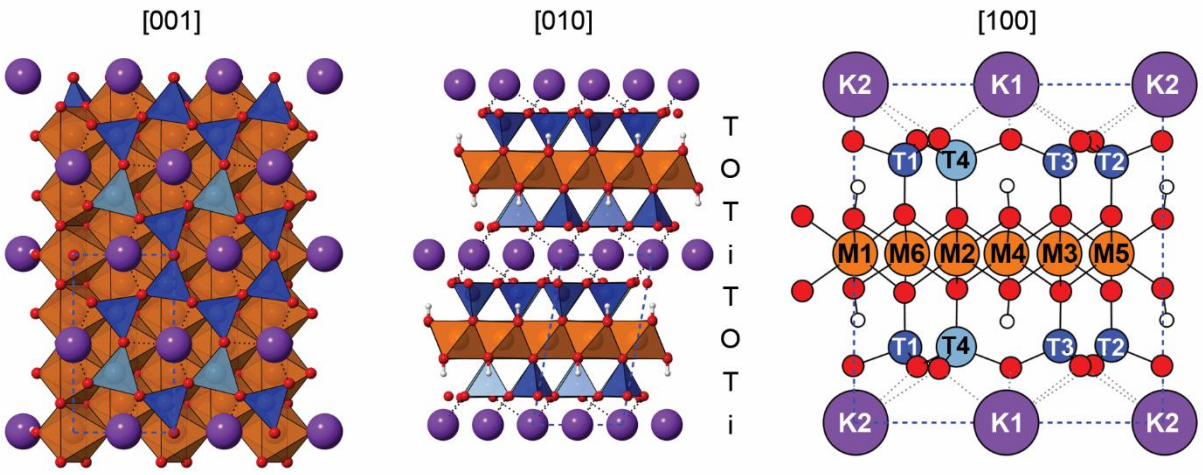

Figure 1. Different views of the 1*M*-phlogopite structure. T and O indicate the tetrahedral and octahedral sheets, respectively, and *i* is the interlayer space with the K^+ ions. The rightmost ball-and-stick image shows the atomic sites of phlogopite.

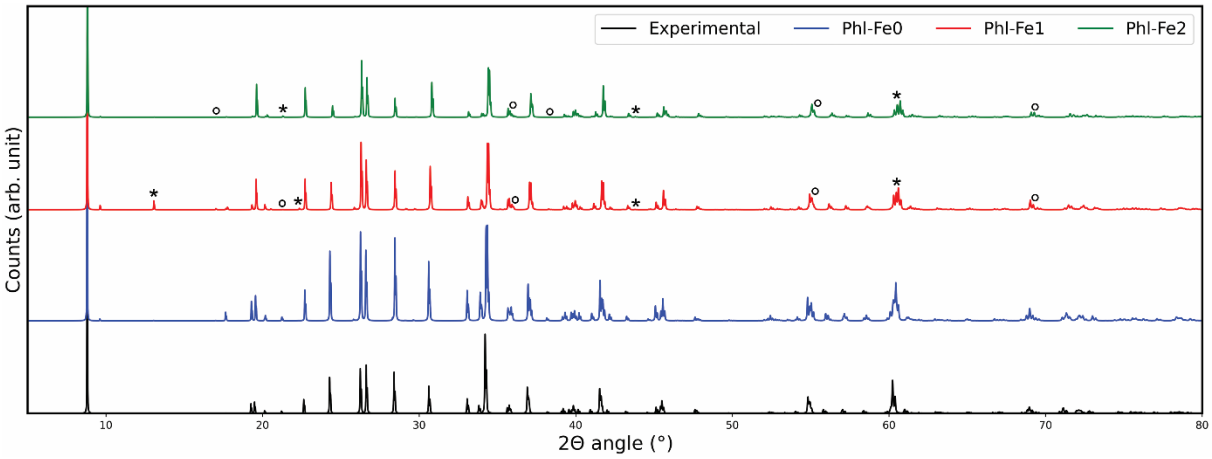

676

677 **Figure 2.** Simulated powder X-ray diffraction patterns of Phl-Fe0 (blue line), Phl-Fe1 (red line) and Phl-Fe2

678 (green line) phlogopite models, compared to the experimental refinement from Ventruti et al. (2009),

679 reported in black line. Asterisks (*) and circles (°) mark the appearance and the disappearance of reflections,

680 respectively, in the Fe-bearing phlogopite models with respect to the stoichiometric one.

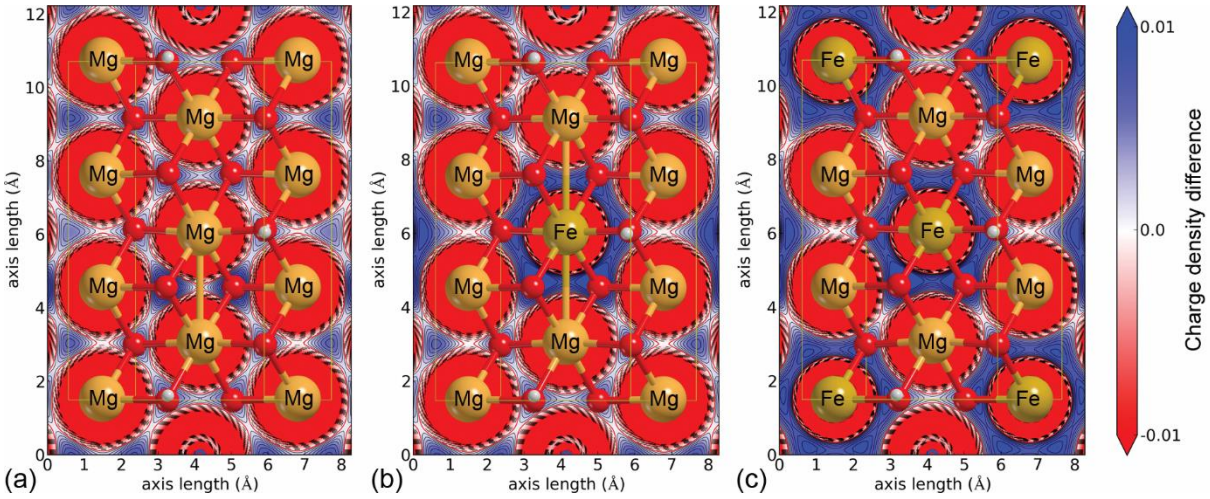

Figure 3. Charge density difference in the octahedral sheet of (a) stochiometric Phl-Fe0, (b) Phl-Fe1 and (c) Phl-Fe2 phlogopite models, calculated with the DFT/B3LYP-D* approach at 0 K. Orange, ochre, red and white indicate Mg, Fe, O and H atoms, respectively.

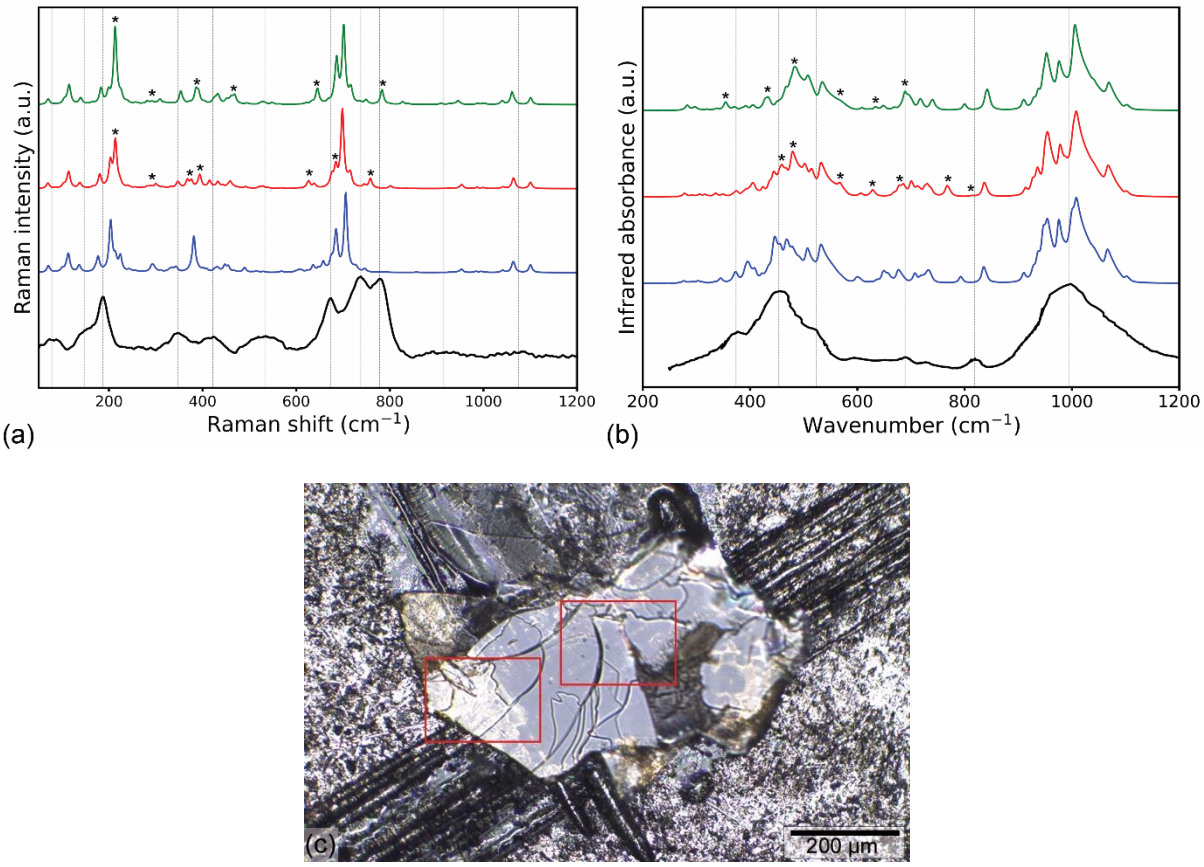

685

686

687 **Figure 4.** (a) Raman and (b) infrared spectra of 1*M* phlogopite polytype models with ideal crystal chemistry
688 $KMg_3(AlSi_3)O_{10}(OH)_2$ (Phl-Fe0, blue line), $KMg_{2.5}Fe_{0.5}(AlSi_3)O_{10}(OH)_2$ (Phl-Fe1, red line) and
689 $KMg_2Fe(AlSi_3)O_{10}(OH)_2$ (Phl-Fe2, green line) as obtained from simulations at the DFT/B3LYP-D* level of
690 theory. In panel (a) a representative Raman spectrum from confocal Raman micro-spectrometry on the BU1-
691 7 sample (black line) is reported, whereas the infrared spectrum shown in panel (b) is from the natural
692 phlogopite sample characterized by Jenkins (1989). The asterisks (*) in both panels (a) and (b) mark the bands
693 that showed the highest spectral variations in terms of position and intensity. Panel (c) shows an optical image
694 of the phlogopite sample, with the red rectangular areas highlighting the zones analysed with Raman
695 spectroscopy.

696

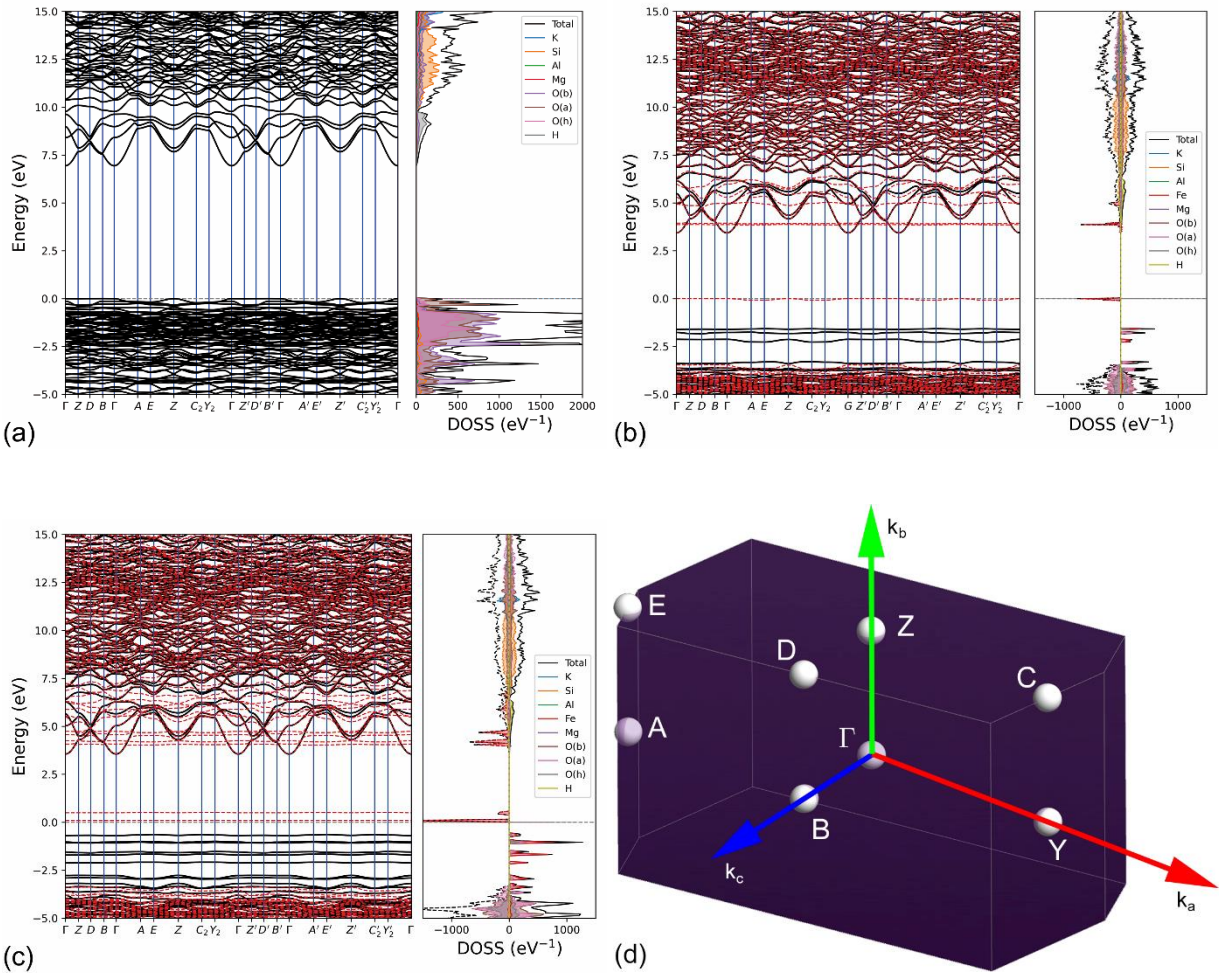

Figure 5. Electronic band structure and atom-projected density of states (DOSS) of (a) Phl-Fe0, (b) Phl-Fe1 and (c) Phl-Fe2 phlogopite-1*M* models in the –5 – 10 eV energy range. The black lines in the band structure are related to the α electrons, whereas the red dashed ones to the β electrons. The density of states associated with the α and β electrons are represented with solid (on the right, positive values) and dashed lines (on the left, negative values), respectively, in the DOSS plots. Panel (d) shows the first Brillouin zone associated with the monoclinic lattice with symmetry *P*2 and its special *k* points.

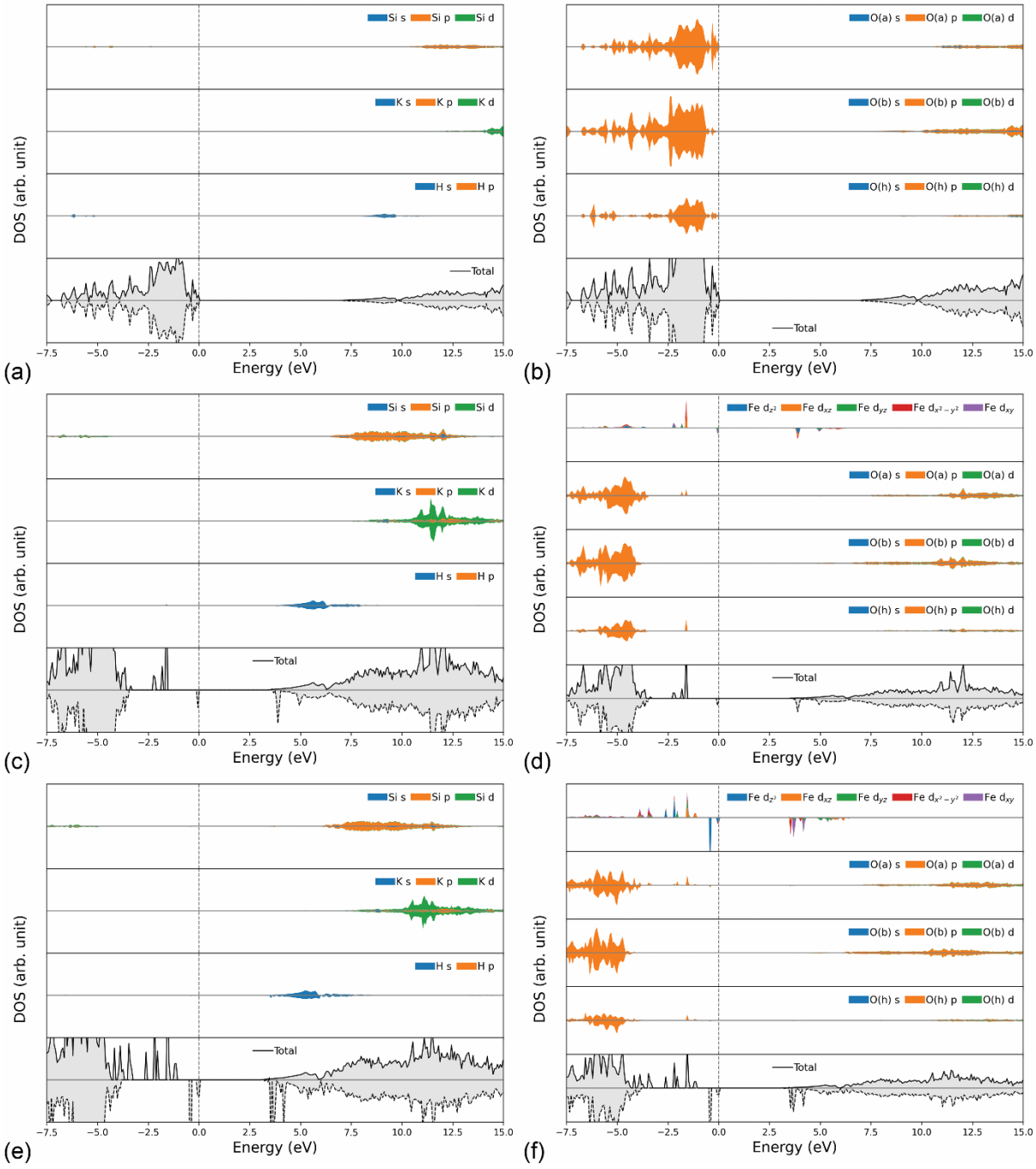

Figure 6. Electronic density of states projected on selected sets of orbitals of the different atoms in the phlogopite-1*M* models. Panels (a,b), (c,d) and (e,f) are related to the Phl-Fe0, Phl-Fe1 and Phl-Fe2 structures, respectively. Solid lines are associated with majority-spin DOS, whereas dashed lines are due to minority-spin DOS. The grey dashed lines indicate the Fermi energy level.

List of tables

Table 1. Crystal structure data of the stoichiometric and Fe-bearing 1*M*-phlogopite from DFT simulations.

	B3LYP-D*			ND	XRD		
	Phl-Fe0	Phl-Fe1	Phl-Fe2		(BU1-1)	Tas 27-2Ba	CA-IT
space group	*P*2	*P2*	*P2*	*C*2/*m*	*C*2/*m*	*C*2/*m*	*C*2/*m*
a (Å)	5.2990	5.2856	5.2740	5.3187	5.3252	5.318	5.337
b (Å)	9.1954	9.1788	9.1692	9.2104	9.2260	9.214	9.240
c (Å)	10.2086	10.1916	10.1689	10.1967	10.2342	10.279	10.237
β (°)	100.228	100.022	99.804	100.148	100.080	100.01	100.02
V (Å^3)	489.52	486.90	484.56	491.69	495.05	496.00	497.1
T_{thick} (Å)	2.2708	2.2720	2.2506	2.232	2.239	2.256	2.25
M_{thick} (Å)	2.1781	2.1621	2.1444	2.141	2.140	2.163	2.20
I_{thick} (Å)	3.3267	3.3300	3.3324	3.372	3.406	3.447	3.39
ψ (°)	58.38	58.39	58.68	58.91	58.91	58.63	58.5
TQE							
T1	1.0015	1.0014	1.0015				
T2	1.0016	1.0015	1.0017				
T3	1.0019	1.0021	1.0021				
T4	1.0013	1.0014	1.0012				
mean	1.0016	1.0016	1.0016	1.000	1.000	1.0004	
Volume T (A^3)							
T1	2.2486	2.2450	2.2460				
T2	2.2523	2.2483	2.2471				
T3	2.2667	2.2638	2.2612				
T4	2.7568	2.7522	2.7479				
mean	2.3811	2.3773	2.3756	2.36	2.336	2.330	2.4
OQE							
M1	1.0076	1.0073	1.0071	1.012	1.012	1.0097	
M2	1.0100	1.0114	1.0123	1.011	1.011	1.0096	
M3	1.0071	1.0085	1.0091				
M4	1.0123	1.0108	1.0106				
M5	1.0085	1.0088	1.0106				
M6	1.0116	1.0125	1.0147				
mean	1.0095	1.0099	1.0107	1.012	1.012	1.0097	
Volume O (A^3)							
M1	11.7415	11.6753	11.1856	11.77	11.85	11.791	12.0
M2	11.8843	11.7671	11.7233	11.59	11.60	11.770	11.9
M3	11.7733	11.7018	11.6801				
M4	11.8359	11.3304	11.2609				
M5	11.7095	11.7014	11.6113				
M6	11.8011	11.7613	11.6588				
mean	11.7909	11.6562	11.5200	11.68	11.73	11.781	12.0

M1 and M4 sites in Fe-bearing phlogopite are occupied by Fe^{2+}. Experimental results from single-crystal X-ray diffraction (SC-XRD) at 100 K (sample BU1-1) and neutron diffraction (ND) at 10 K were taken from the works of Lacalamita and co-workers (2012) and Ventruti et al. (2009), respectively. Tas 27-2Ba sample was characterized in the study of Brigatti and collaborators (1996), whereas the CA-IT phlogopite was refined by Comodi et al. (2004). T_{thick}, M_{thick}, and I_{thick} are tetrahedral sheet thickness (calculated from the *z* coordinates of the basal and apical oxygen atoms), the octahedral sheet thickness (calculated from the *z* coordinates of the apical and hydroxyl O atoms) and interlayer thickness (calculated from the *z* coordinates of the basal oxygen atoms), respectively. TQE and OQE are the tetrahedral and octahedral quadratic elongations, respectively (Robinson et al., 1971).

716 **Table 2.** Mean bond lengths and interlayer distances (Å) in the different cationic sites of 1*M* phlogopite obtained from

717 different DFT simulations, compared to previous experimental results.

	B3LYP-D*			**SC-XRD**			**ND[4]**
	Phl-Fe0	Phl-Fe1	Phl-Fe2	(BU1-1)[1]	Tas 27-2Ba[2]	CA-IT[3]	
Tetrahedral sheet							
⟨Si1 – O⟩	1.6374	1.6366	1.6366				
⟨Si2 – O⟩	1.6385	1.6376	1.6372				
⟨Si3 – O⟩	1.6421	1.6416	1.6407				
⟨Al – O⟩	1.7524	1.7516	1.7503				
⟨T – O⟩	1.6676	1.6669	1.6662	1.657	1.656	1.67	1.663
Octahedral sheet							
⟨M1 – O⟩	2.0726	2.0683	2.0391	2.068	2.078	2.09	2.068
⟨M2 – O⟩	2.0832	2.0778	2.0764	2.084	2.077	2.09	2.079
⟨M3 – O⟩	2.0739	2.0713	2.0705				
⟨M4 – O⟩	2.0826	2.0511	2.0473				
⟨M5 – O⟩	2.0717	2.0714	2.0682				
⟨M6 – O⟩	2.0802	2.0788	2.0749				
⟨M – O⟩	2.0774	2.0698	2.0627	2.073		2.09	2.072
Interlayer							
⟨K1 – O⟩	3.1558	3.1510	3.1483		3.172		
⟨K2 – O⟩	3.1167	3.1144	3.1112		3.172		
⟨K – O⟩	3.1363	3.1327	3.1297	3.164	3.172		3.153
Hydroxyl groups							
⟨O – H⟩	0.9555	0.9560	0.9563				

1 – room temperature (298 K) single-crystal XRD refinement of Lacalamita et al. (2012); 2 – single-crystal XRD results of Brigatti and co-workers (1996); 3 – single-crystal XRD refinement of Comodi et al. (2004); 4 – neutron diffraction refinement at 10 K by Ventruti et al. (2009). T and M represent the generic tetrahedral and octahedral sites, respectively.

718

719 **Table 3.** Irreducible representations of the normal modes of the 1*M* polytype of phlogopite according to the site

720 symmetry.

1*M* polytype (s.g. *P*2)			
Atom	Wyckoff	*A*	*B*
K	1a	1	2
K	1c	1	2
Mg1/Fe1	1b	1	2
Mg2	1b	1	2
Mg3	1b	1	2
Mg1/Fe4	1d	1	2
Mg5	1d	1	2
Mg6	1d	1	2
Si1	2e	3	3
Si2	2e	3	3
Si3	2e	3	3
Al1	2e	3	3
O(b)1	2e	3	3
O(b)2	2e	3	3
O(b)3	2e	3	3
O(b)4	2e	3	3
O(b)5	2e	3	3
O(b)6	2e	3	3
O(a)1	2e	3	3
O(a)2	2e	3	3
O(a)3	2e	3	3
O(a)4	2e	3	3
O(h)1	2e	3	3
O(h)2	2e	3	3
H	2e	3	3
H	2e	3	3

721

722

Table 4. Infrared and Raman vibrational frequencies ν (cm^{-1}) related to the irreducible representation *A* of stoichiometric (Phl-Fe0) and iron-bearing 1M-phlogopite models (Phl-Fe1 and Phl-Fe2), calculated from DFT/B3LYP-D* simulations. Transverse optic (TO) and longitudinal optic (LO) frequencies, and IR and Raman intensities for each mode are reported.

Phl-Fe0				Phl-Fe1				Phl-Fe2			
ν_{TO}	$\Delta\nu_{LO-TO}$	*IR*	*R*	ν_{TO}	$\Delta\nu_{LO-TO}$	*IR*	*R*	ν_{TO}	$\Delta\nu_{LO-TO}$	*IR*	*R*
70.7	0.1	0.2	93.8	69.7	0.1	0.6	74.8	70.0	0.0	0.1	71.2
111.8	6.1	24.5	60.6	111.8	6.0	44.3	10.2	112.9	6.1	28.4	8.5
113.0	-0.3	5.7	218.6	113.7	-0.1	1.6	228.1	114.4	-0.1	0.8	256.3
136.4	0.0	0.2	94.6	137.8	0.0	0.1	70.8	139.4	0.0	0.0	74.9
171.3	1.5	11.2	34.4	166.0	1.4	14.4	12.8	163.3	1.3	8.2	13.1
176.9	0.2	1.2	273.6	180.5	0.0	0.2	263.1	183.0	0.0	0.2	300.3
203.7	0.0	0.0	709.7	203.1	0.1	2.0	351.6	199.0	0.0	0.0	157.3
213.7	0.0	0.1	162.6	213.8	0.1	2.0	628.9	213.4	0.0	0.1	1000.0
224.5	0.0	0.2	201.6	223.5	0.0	0.3	60.7	226.1	0.1	0.8	96.1
254.3	0.0	0.3	15.8	255.7	0.4	8.7	8.3	256.2	0.0	0.3	17.2
259.4	0.0	0.0	10.6	258.0	0.0	0.0	11.0	261.2	0.1	0.7	15.0
285.4	0.6	11.5	2.2	286.3	0.1	2.3	5.5	286.0	0.0	0.3	1.4
291.9	0.8	14.7	59.8	292.0	1.3	34.5	7.8	289.9	0.3	6.3	15.6
295.6	0.2	3.3	55.7	300.3	0.2	3.9	52.9	296.3	2.4	36.0	2.0
310.8	0.6	12.3	12.6	306.4	0.2	6.8	7.7	308.9	0.0	0.0	47.0
329.1	0.1	1.9	39.0	315.4	1.7	45.8	15.8	318.9	1.0	15.9	17.9
334.8	0.0	0.9	9.2	332.4	0.1	2.2	26.1	331.2	0.4	6.8	15.9
340.1	0.0	1.2	17.5	346.5	0.3	9.8	73.6	336.9	0.1	1.9	10.3
343.1	0.8	20.7	59.0	354.4	0.1	3.2	5.7	353.4	0.1	1.8	166.9
363.1	0.0	0.0	8.2	367.6	0.3	14.5	100.4	371.7	0.8	20.7	13.6
369.3	1.5	66.0	4.4	371.5	0.7	34.0	3.2	376.5	0.0	0.0	5.0
375.6	0.3	11.5	12.1	376.3	0.7	31.1	87.1	385.9	0.2	6.5	163.2
381.4	0.1	5.0	452.5	391.2	0.8	63.9	16.5	391.5	1.6	50.2	123.9
390.3	1.7	262.8	23.1	394.3	0.5	32.9	153.0	403.9	0.7	23.0	11.7
393.6	15.4	222.1	2.1	403.3	5.9	321.7	1.5	413.1	0.0	1.2	6.5
401.5	-0.2	7.0	31.5	415.0	0.9	36.5	94.9	423.3	0.3	26.2	36.2
424.8	0.6	20.8	1.5	422.7	2.0	98.9	11.8	427.4	2.7	215.3	43.4
433.7	4.4	127.3	21.8	436.1	1.4	144.3	11.5	432.5	7.1	135.6	42.2
435.3	-0.2	16.6	13.8	442.2	10.2	293.0	26.6	450.6	0.7	30.0	44.3
447.5	0.4	22.1	140.4	446.4	-1.6	139.0	15.3	455.7	2.1	77.1	44.1
455.8	3.3	272.3	23.3	460.4	0.2	18.3	69.4	468.7	0.6	54.4	112.2
466.0	108.0	599.4	7.9	467.0	2.4	264.2	22.7	472.9	1.0	101.8	3.6
468.8	0.0	11.0	8.3	477.4	104.1	1000.0	4.8	480.5	108.6	777.3	1.7
489.8	-1.0	32.8	83.3	492.0	-0.1	7.0	29.9	496.7	-0.4	19.4	11.0
515.8	-0.5	5.2	18.9	521.2	0.0	0.6	18.8	527.9	0.0	1.8	7.6
523.5	0.3	0.7	2.3	528.4	0.0	0.5	23.2	528.4	-4.0	31.4	10.2
528.0	-5.2	57.7	6.7	530.6	-5.4	114.0	5.5	534.2	-3.1	81.0	14.2
531.4	0.0	0.9	5.0	539.7	0.0	0.4	15.1	548.7	0.0	0.2	33.6
598.2	7.6	31.8	17.9	605.6	3.5	27.4	5.3	608.1	2.9	11.0	1.2
611.8	0.1	0.2	31.6	627.6	6.9	63.3	3.8	633.4	3.0	24.0	34.4
636.2	1.7	15.3	119.0	638.8	0.1	0.6	72.3	647.6	5.0	33.1	36.3
657.7	2.9	41.3	180.0	675.3	0.8	25.1	119.6	681.2	1.1	22.5	81.3
674.9	15.4	123.1	146.8	684.6	7.6	146.1	246.4	686.5	5.8	51.4	522.7
685.5	-0.5	2.6	460.8	698.7	3.9	38.4	1000.0	701.6	1.9	15.9	939.7
705.8	2.8	22.7	1000.0	715.8	2.6	48.7	157.8	717.3	7.5	63.3	137.9
717.4	3.4	26.8	10.6	724.8	9.3	77.6	5.3	736.2	3.8	22.3	31.1
727.9	5.7	27.2	73.2	745.2	0.2	1.3	38.8	749.4	0.5	2.8	47.2
746.5	0.0	0.1	48.0	758.6	0.1	1.3	208.3	783.4	0.3	3.5	299.7
783.4	0.0	0.1	3.2	801.1	0.0	0.0	51.4	827.5	0.1	2.4	53.2
857.1	0.1	2.4	6.8	851.5	0.0	0.8	1.4	855.9	0.1	1.1	2.4
935.5	5.6	357.5	4.9	934.5	7.0	626.6	7.1	936.4	3.2	287.6	10.0
944.9	0.2	7.8	11.6	948.3	0.1	8.8	10.2	945.6	18.9	403.2	45.5
953.2	22.3	518.2	43.1	953.7	20.8	705.5	48.2	951.1	0.0	0.1	11.2
995.2	1.9	91.8	19.9	998.4	1.4	152.4	14.8	999.3	0.9	146.1	19.4
1007.0	103.2	539.7	4.9	1007.0	101.2	864.6	3.2	1004.4	88.8	660.3	6.0
1041.0	-0.8	11.8	26.6	1042.3	-0.4	9.2	18.6	1040.4	-0.6	10.0	34.0
1062.8	-4.0	23.3	102.5	1063.7	-4.7	38.4	107.2	1061.2	-1.6	6.4	161.1
1065.6	-0.8	13.8	75.1	1065.9	-0.7	25.1	50.8	1067.5	-3.5	30.1	26.2

1100.7	-6.8	10.3	118.6	1100.5	-5.9	11.6	92.3	1101.0	8.4	11.2	93.9
3761.1*	0.1	5.6	372.0	3771.8*	0.0	3.0	482.9	3755.4*	0.1	3.6	436.4
3785.5*	0.0	2.1	439.9	3773.4*	0.1	7.7	386.0	3761.6*	0.0	1.4	658.0

Notes: modes marked with an asterisk (*) were corrected for anharmonicity.

Table 5. Infrared and Raman vibrational frequencies ν (cm^{-1}) related to the irreducible representation *B* of stoichiometric (Phl-Fe0) and iron-bearing 1M-phlogopite models (Phl-Fe1 and Phl-Fe2), calculated from DFT/B3LYP-D* simulations.

Phl-Fe0			**Phl-Fe1**			**Phl-Fe2**		
ν_{TO}	*IR*	*R*	ν_{TO}	*IR*	*R*	ν_{TO}	*IR*	*R*
85.8	2.7	10.4	86.1	2.5	15.4	86.8	1.7	6.9
100.0	2.9	70.3	103.0	1.9	75.0	104.7	1.0	82.9
106.9	24.7	35.2	109.6	29.5	17.2	110.6	28.0	17.7
114.0	4.3	138.2	114.6	3.7	129.3	116.0	3.2	148.8
131.8	85.0	0.0	133.6	93.3	0.2	135.0	86.3	0.1
139.6	1.0	6.7	140.8	0.3	6.7	142.2	0.1	10.1
144.8	0.8	1.9	151.9	1.0	1.3	157.6	2.5	4.9
170.4	12.3	8.0	164.6	8.5	5.6	165.0	8.3	6.1
186.2	1.8	5.3	178.8	3.0	3.7	169.7	0.8	8.8
190.5	2.2	9.9	192.3	2.8	5.9	189.0	0.1	1.9
210.3	1.4	6.9	202.9	2.0	2.7	196.9	1.5	1.4
218.0	1.7	14.9	221.0	1.6	17.3	223.5	1.4	23.4
236.1	1.5	3.2	239.4	1.8	21.7	238.6	3.0	9.4
242.9	0.1	42.6	241.8	0.1	17.3	239.0	1.5	32.3
247.0	3.7	13.8	244.8	2.8	5.1	244.5	0.1	1.6
267.3	5.0	12.4	271.0	3.6	14.0	272.9	5.5	8.8
275.4	25.0	7.5	277.4	49.8	2.2	281.9	43.4	19.1
281.3	1.5	4.1	282.0	0.9	34.7	282.0	34.1	39.8
290.3	0.1	37.8	289.5	1.7	28.9	293.3	1.1	30.6
299.5	3.9	16.0	298.2	3.1	7.5	297.9	16.7	5.4
303.0	29.7	12.0	305.6	31.4	12.6	302.7	4.1	17.4
310.5	1.9	19.0	310.8	0.8	5.1	309.5	5.0	45.7
322.4	0.0	11.1	323.2	7.2	9.6	324.4	0.4	16.6
333.9	13.6	57.4	335.2	56.4	5.3	338.2	23.5	1.1
345.0	67.3	25.6	349.2	20.2	51.0	347.7	0.9	0.1
353.5	2.1	1.6	350.0	8.4	1.1	353.3	132.2	0.3
363.1	7.1	2.9	367.1	12.7	0.7	358.8	3.9	25.4
372.5	150.5	18.4	374.0	63.3	2.9	370.2	23.2	4.6
385.9	9.3	11.7	386.6	36.7	6.5	384.6	11.7	1.0
393.4	0.0	3.2	391.9	29.3	10.5	391.6	20.2	5.7
397.4	60.8	14.9	398.1	61.6	5.0	403.1	8.7	12.4
408.6	160.2	52.1	407.9	46.5	12.2	405.1	39.8	10.2
421.4	74.2	0.1	424.4	75.0	3.0	426.6	12.3	3.0
425.5	5.2	42.5	432.2	4.5	118.4	433.2	10.3	100.0
430.4	41.3	59.8	435.3	93.8	10.0	436.5	10.8	26.4
442.4	697.4	7.0	443.6	222.0	7.4	449.7	77.5	3.3
444.8	444.5	0.7	454.0	493.6	35.3	461.5	180.8	114.9
454.8	30.5	93.1	458.0	328.7	66.2	465.5	379.6	23.5
469.7	37.2	5.9	473.5	61.2	9.3	474.5	333.8	7.0
477.8	114.1	3.9	476.9	105.5	8.1	485.0	150.6	2.3
505.5	248.8	6.9	501.3	211.6	5.7	493.4	24.0	13.8
511.7	15.9	4.8	513.3	125.1	0.3	506.6	245.7	1.8
519.9	9.0	0.0	521.5	0.7	10.2	524.0	3.7	26.4
523.6	21.2	0.7	524.3	9.7	0.4	528.5	4.5	5.5
530.4	243.7	6.7	529.9	192.3	11.4	531.5	139.3	16.9
568.5	1.8	27.7	566.3	39.2	12.5	564.6	3.7	8.8
605.8	9.3	50.9	622.3	3.6	16.4	621.3	4.7	22.8
624.1	4.4	25.2	626.6	7.2	147.1	645.1	1.7	286.2
647.5	103.7	66.4	667.5	29.0	9.6	668.4	22.2	45.7
664.3	5.6	21.3	677.0	79.0	102.2	688.1	138.3	2.0
682.4	3.0	139.7	699.7	121.1	1.9	695.2	118.8	3.3
707.0	54.5	7.8	710.7	62.0	74.4	715.1	45.2	76.1
723.1	28.8	36.5	730.4	65.7	7.3	739.7	84.6	0.1
732.0	71.3	2.4	736.7	38.5	4.2	749.2	1.1	1.5
734.5	16.0	4.4	765.9	113.5	4.1	799.2	72.1	8.9

791.9	56.6	13.1	813.0	7.6	9.6	839.0	169.3	9.4
834.2	202.0	0.0	835.4	196.1	5.9	841.8	137.6	5.5
909.7	106.0	1.7	912.9	96.8	1.9	909.2	138.1	28.1
927.2	120.1	6.2	925.8	161.8	7.6	927.8	95.1	18.1
945.4	873.5	0.2	948.9	926.3	0.2	951.5	842.3	0.2
974.3	1000.0	1.0	976.4	1000.0	5.6	974.3	1000.0	0.4
984.0	50.3	24.3	986.5	102.6	22.3	987.7	18.4	24.8
998.7	678.2	4.6	1001.6	715.5	5.6	1002.5	657.0	5.8
1036.6	7.0	0.8	1037.2	5.4	2.3	1038.9	7.4	18.0
1046.4	1.9	0.2	1047.9	0.3	0.5	1049.0	1.3	0.3
1064.3	62.0	0.9	1066.1	63.9	7.5	1066.6	63.5	5.5
3761.0*	42.9	24.0	3772.1*	28.7	5.5	3755.2*	35.2	16.9
3785.6*	31.5	6.1	3773.2*	51.6	18.7	3762.0*	32.2	5.0

Notes: modes marked with an asterisk (*) were corrected for anharmonicity.

Table 6. Most intense bands in the experimental Raman and infrared spectra of phlogopite, together with the related theoretical bands and the assignment to specific normal modes.

	ν_{exp} (cm^{-1})	ν_{DFT} (cm^{-1})	Assignment
Raman[1]	78	114	TOT sliding
	147	180	Mg–O(a)–Mg
	187	205	Mg–O(a)–Mg
	347	345	O–Mg–O
	422	456	Mg–O(h)
	533	530	Mg–O(a)
	674	686, 707	O(b)–Si – O(a) and O(b)–Al–O(a) "umbrella"
	738	746	Si – O(b)
	778	792	Si – O(b)
	915	927	Si – O(a)
	1075	1066, 1101	Si – O(a) and Si – O(b)
Infrared[2]	374	390	O–Mg–O + Mg – O
	453	463	Mg – O(h)
	523	530	Mg – O(a)
	689	706	O(b) – Si – O(a) "umbrella"
	819	834	Al – O(a)
	994	935, 976, 999, 1008	Si – O(a) and Si – O(b)

1 – present work; 2 – Jenkins (1989).

Table 7. Static relative permittivity ε, refractive index n and high-frequency relative permittivity ε_{HF} of the different phlogopite models along the principal Cartesian directions, as obtained from DFT/B3LYP-D* simulations at 0 K.

		Phl-Fe0			**Phl-Fe1**			**Phl-Fe2**		
		xx	*yy*	*zz*	*xx*	*yy*	*zz*	*xx*	*yy*	*zz*
ε										
	B3LYP-D*[1]	6.58	6.43	5.08	6.31	6.30	5.02	6.07	6.13	4.99
	B3LYP[2]	6.12	6.31	4.74						
	Exp[3]	6.80	-	-						
n										
	B3LYP-D*[1]	1.49	1.52	1.52	1.51	1.54	1.54	1.52	1.56	1.56
	B3LYP[2]	1.44	1.45	1.41						
	Exp[4]	1.52	1.55	1.55						
ε_{HF}										
	B3LYP-D*[1]	2.32	2.32	2.22	2.37	2.37	2.26	2.43	2.42	2.31
	B3LYP[2]	2.08	2.09	2.41						

1 – present work; 2 – theoretical results of Timon and collaborators (2013); 3 – experimental data from Gudkov and Metsik (1973), measured in the direction parallel to cleavage; 4 – experimental data from Bisdom et al. (1982).